2010

X-ray diffraction applications in thin films and (100) silicon substrate stress analysis

James D. Rachwal
University of South Florida

X-Ray Diffraction Applications

in Thin Films and (100) Silicon Substrate Stress Analysis

by

James D. Rachwal

A thesis submitted in partial fulfillment
of the requirements for the degree of
Master of Science in Mechanical Engineering
Department of Mechanical Engineering
College of Engineering
University of South Florida

Major Professor: Dr. Alex A. Volinsky, Ph.D.
Dr. Craig Lusk, Ph.D.
Dr. Delcie Durham, Ph.D.

Date of Approval:
April 7, 2010

Keywords: Thin films, Residual stress, X-Ray diffraction,
$Sin^2\psi$ technique

Table of Contents

List of Tables v

List of Figures vi

ABSTRACT ix

Chapter 1. X-Ray Mirrors 1

1.1 Introduction to X-Ray Mirrors 1

1.2 Distortions in X-Ray Mirrors 2

1.3 Stress in the X-Ray Mirror Thin Film 3

Chapter 2. Introduction to Stress in Thin Films 4

2.1 Origin of Stress in Thin Films 4

2.2 Overview of Thin Film Deposition 4

2.3 Mechanics of (100) Silicon Substrate 5

2.3.1 Crystallographic Properties of (100) Silicon 5

2.3.2 Elastic Properties of (100) Silicon 7

Chapter 3. Stress Characterization Techniques 9

3.1 X-Ray Diffraction 9

3.1.1 Lattice Parameter and Bragg's Law 9

3.1.2 $Sin^2\psi$ Technique 11
3.1.3 Strain Transformation 13
3.1.4 $Sin^2\psi$ Equation 20
3.1.5 Calculation of Stress Using $Sin^2\psi$ 22
3.1.6 $Sin^2\psi$ Example 24

3.2 Curvature Methods 25

3.2.1 Stoney's Equation 25
3.2.2 Curvature Measuring Techniques 26

Chapter 4. In-Situ Bending Experiments in XRD 29

4.1 Four-Point Bending Apparatus Design 29
4.2 System Alignments 31

4.2.1 Vertical Alignment 31
4.2.2 Zeroing the Sample 33
4.2.3 Rocking Scan 34

4.3 Sources of Error 36

4.3.1 Errors Due to Change in Height 37

4.4 Depth of X-Ray Penetration 38

4.4.1 Basis of X-Ray Absorption 38
4.4.2 Depth of Attenuation 38

4.5 Scanning Procedure 40

4.6 Peak Determination 40

4.6.1 Peak Height....40

4.6.2 Peak Determination Functions....41

4.6.3 Procedure for Peak Determination....42

4.7 Error Corrections 44

4.8 In-Situ XRD results 45

4.9 Comparison of XRD Results with Calculated Bending Strains 47

Chapter 5. System Calibration and Experiment with IONIC-System Stress-Gauge 49

5.1 IONIC-Systems Profile Calibration....49

5.1.1 Factory Calibration 49

5.1.2 Taking Readings 49

5.1.3 Profile Calculation....53

5.2 IONIC-System Experiment....54

5.2.1 IONIC-Systems Stress-Gauge Readings....54

5.2.2 Wafer Deflection Equation 55

5.2.3 Variation Caused by Anisotropic Properties....57

5.2.4 IONIC Stress-Gauge Error Analysis....58

5.2.5 Wafer Deflection Results 59

Chapter 6. Conclusions and Future Work 60

References....62

Apendix A....68

A-1 IONIC-Systems Stress-Gauge 68

A-1.1 IONIC-Systems Stress-Gauge Calibration Setup 74

A-1.2 Taking a Measurement on the IONIC-Systems Stress-Gauge 76

List of Tables

Table 1. $Sin^2\psi$ Data for Tungsten Film on a (100) Silicon Wafer. 24

Table 2. Mechanical Properties of Tungsten. 25

Table 3. Comparison of Calculated and XRD Strain Results. 48

Table 4. Results From Stress-Gauge Profile Calibration. 54

Table 5. Readings From IONIC-Systems Stress-Gauge for Various Weights Added, and the Corresponding Displacements. 55

Table 6. Wafer Deflection Measurements and Calculations. 59

Table 7. Errors From Deflection Calculations. 59

List of Figures

Figure 1. Illustration of a Göbel Mirror....1

Figure 2. Illustration of a Göbel mirror distorted by thermal expansion....3

Figure 3. Crystal Structure of Silicon....5

Figure 4. (a) Identifying features of single crystal silicon wafers....6

Figure 5. Determination of lattice spacing using Bragg's law. 11

Figure 6. Coordinate System Used for the $\sin^2\psi$ Technique. 12

Figure 7. Basic principles of $\sin^2\psi$ stress determination. 13

Figure 8. ε_x Component of the 3D-Strain Transformation to the $\varepsilon_{x'}$ Axis....14

Figure 9. ε_y Component of the 3D-Strain Transformation to the $\varepsilon_{x'}$ Axis....15

Figure 10. ε_z Component of the 3D-Strain Transformation to the $\varepsilon_{x'}$-Axis. 16

Figure 11. γ_{xz} Component of the 3D-Strain Transformation to the $\varepsilon_{x'}$-Axis. 17

Figure 12. (a) γ_{xz} Component of the 3D-Strain Transformation to the $\varepsilon_{x'}$-Axis. (b) Close-Up of the Strain Transformation Components. 18

Figure 13. (a) γ_{yz} Component of the 3D-Strain Transformation to the $\varepsilon_{x'}$-Axis. (b) Close-Up of the Strain Components....19

Figure 14. $d_{\phi\psi}$ vs. $\sin^2\psi$ for (a) Linear Behavior, (b) ψ-Splitting Behavior, and (c) Oscillatory Behavior. Adapted from [24]. 21

Figure 15. Example of a $d_{\phi\psi}$ vs. $\sin^2\psi$ Plot for Tungsten Film....23

Figure 16. Forces Acting on a Cross-Sectional Area Act as the Basis of Stoney's Equation. 25

Figure 17. IONIC Stress-Gauge Measurement. 26

Figure 18. (a) 4-Point Bending Fixture. (b) Description of Parts. 29
Figure 19. Constant Radius of Curvature Between Inner Bending Points on a 4-Point Bending Setup. 30
Figure 20. Alignment Test for Vertical Position. 31
Figure 21. Illustration of an Alignment Test, with the Wafer Too L4ow. 32
Figure 22. Illustration of an Alignment Test with the Wafer Too High. 32
Figure 23. The 2θ-Scan with a Misaligned Wafer. 34
Figure 24. Relative Intensity of Diffracted X-Rays. 35
Figure 25. Rocking-Scan Used to Determine the Alignment of the Wafer. 35
Figure 26. Using an Offset Angle to Correct for Angular Alignment. 36
Figure 27. Source of Error Due to Changing Height of Wafer Sample. 37
Figure 28. Schematic Representation of a Diffraction Reflection, (a) Before, and (b) After Stripping Cu[kα2] Off of the Raw Data. 43
Figure 29. Four-Point Bending Setup for X-Ray Diffraction with Copper Powder Added. 44
Figure 30. Illustration of Copper Powder Correction. 45
Figure 31. Raw data from the X-ray diffraction scans, after adjusting for copper 220 XRD Reflections, Showing Cu[kα1], and Cu[kα2] Peaks 46
Figure 32. Setup of Digital Indicator on the IONIC-Systems Stress-Gauge for the Profile Calibration. 51
Figure 33. Data Used in Stress-Gauge Profile Calibration. 53
Figure 34. (a) Weight Producing a Small Circular Area Load on the Wafer. (b) Lip Produced by Machining Process. (c) Load from Weight Concentrated Along Outer Edge of Weight-Flat. 56
Figure 35. Back panel of IONIC-systems stress-gauge 69

Figure 36. Top of IONIC-Systems stress-gauge. 70

X-Ray Diffraction Applications
in Thin Films and (100) Silicon Substrate Stress Analysis

James D. Rachwal

ABSTRACT

Silicon is used as a substrate for X-ray mirrors for correct imaging. The substrate needs to be mechanically bent to produce a certain curvature in order to condition and focus the X-ray beam. The X-rays impinge a mirror at very shallow angles, in order to reduce the amount of intensity loss in the diffraction process. The X-ray mirrors need to be bent to an extremely precise profile, and even small distortions from this profile can reduce the effectiveness of the X-ray mirrors. The X-rays that impinge on the mirror also produce large amounts of heat that can change the temperature of the substrate, resulting in its thermal expansion and distortion. By measuring the distortions in-situ caused by these temperature changes it may be possible to correct for these errors. A four-point bending fixture was designed for in-situ X-ray bending experiments in order to measure the distortions to the (100) silicon sample caused by the bending setup. By being able to measure the distortion caused by the setup, in like manner it would be possible to measure distortion caused by thermal expansion. Several alignments were needed in order to obtain accurate results, including adding copper powder on top of the sample. The copper powder that was added is not under stress, and therefore will not shift its reflection peak when the sample is under bending stress, thus serving as a reference in order to make corrections. The strain results were then compared to values calculated from mechanical deflections from bending. Despite the efforts to control accuracy, a significant variation appeared in the values when the top surface was in

compression. As an alternative an IONIC stress-gauge was used to measure the deflections of the sample rather than calculate them. Another alternative was to calculate the deflection of the substrate by first determining the stress in the layer deposited onto the mirror's substrate by using $\sin^2\psi$ technique, then using Stoney's equation to determine the change in curvature of the substrate, with the stress in the layer being known. Several tests were performed to demonstrate the ability to measure these deflections.

Chapter 1.
X-Ray Mirrors

1.1 Introduction to X-Ray Mirrors

Silicon is used as a substrate for X-ray mirrors commonly known as Göbel mirrors [1]. Göbel mirrors require extremely precise profiles in order to be effective in X-ray mirrors [2]. Commonly these mirrors are bent into either parabolic or elliptical shapes [3]. The shape of the mirror is used to focus the X-ray beam, meaning that the X-rays will reflect off the mirror as parallel beams. In this manner the X-rays are focused at an infinite distance [2,3], as shown in Figure 1.

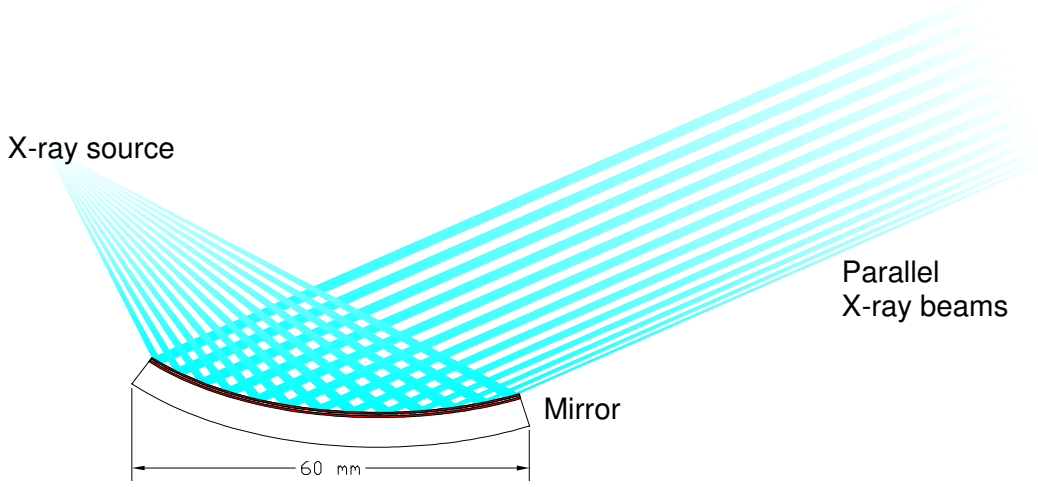

Figure 1. Illustration of a Göbel Mirror.

In a synchrotron "white beam" X-rays are generated and diffract off a monochromator that leaves one frequency, and then reflect off the Göbel mirror. The X-

rays that are diffracted off the monochromator tend to get attenuated to some lesser degree [4]. Any amount of attenuation to the intensity of the diffracted rays gets absorbed by the mirror in the form of heat energy [4], and this heat energy can have detrimental effects on the performance of the mirror, including possibly damaging the mirror [5]. Additional heat energy causes thermal expansion of the mirror, and if the temperature of the mirror is allowed to exceed a certain amount a chemical reaction will occur that will permanently damage the mirror [6]. This thesis focuses on the concerns of distortions to the mirror due to thermal expansion. The X-rays are reflected off the mirror at extremely shallow angles [7,8], which causes a very small loss of intensity to the reflected X-rays, and therefore a minimal amount of heat energy will be absorbed by the mirror [7]. The reason for this is that most materials have a critical angle, below which a reflected beam experiences little loss of the energy, and almost none of the energy will be absorbed by the material [7]. The angle at which X-rays are reflected off the mirror is very close to, but steeper than the critical angle; as a result some of the energy gets absorbed by the mirror. To compensate for the energy being absorbed by the mirror, Göbel mirrors are cooled with liquid nitrogen [9].

1.2 Distortions in X-Ray Mirrors

Despite the efforts to control the temperature of the X-ray mirrors, thermal expansion still occurs. The distortions caused by thermal expansion can affect the performance of the X-ray mirrors [10], as shown in Figure 2. As a means to determine these strains, a four-point bending fixture was designed for in-situ X-ray bending experiments.

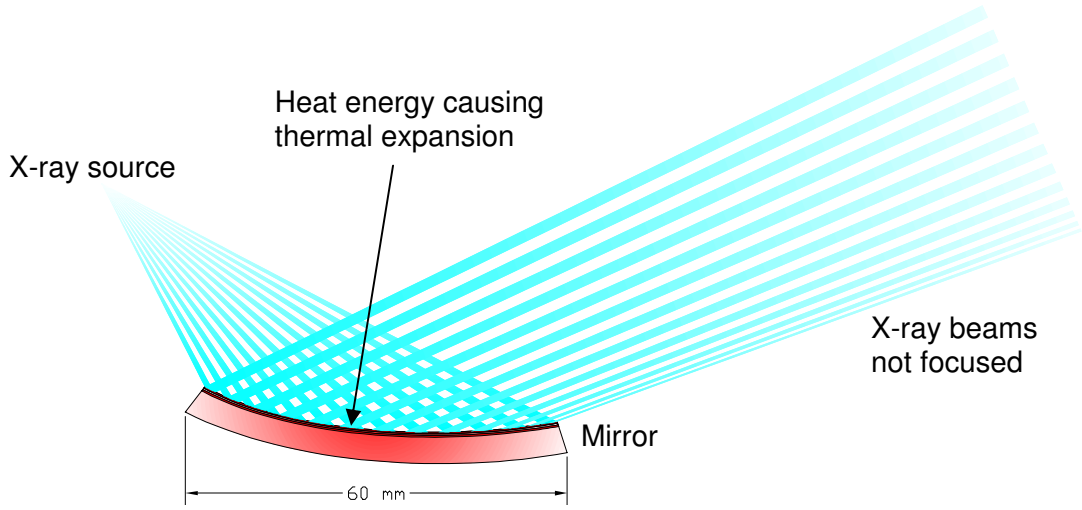

Figure 2. Illustration of a Göbel mirror distorted by thermal expansion.

1.3 Stress in the X-Ray Mirror Thin Film

X-ray mirrors have multiple layers deposited on them, most commonly these are alternating layers of In_2O_3/Ag, W/B_4C, Mo/B_4C, Re/Si, Re/C, W/Si, W/C, Ta/Si, W/Be, Mo/Be, Mo/Si, Mo/C, Ni/C, Au/C, AuPd/C, ReW/B, ReW/C, Al/Be or V/C [11]. These layers may be amorphous, or crystalline [11]. A stress in a film deposited onto a substrate will cause the substrate to bend [12]. Stoney's equation is used to determine the stress in the film, based on the change in curvature due to the stress [32], however if the stresses were to be determined, then from the stress in the film, the change in curvature of the substrate could be determined. The stress in the film could be determined by using $\sin^2\psi$ method.

Chapter 2.
Introduction to Stress in Thin Films

2.1 Origin of Stress in Thin Films

Stress originates in thin films or substrates due to substrate-film differences in thermal expansion, or due to epitaxial mismatch [13-16]. For stresses due to thermal expansion, if substrate-film are in equilibrium at one temperature, and there is a change in temperature, the film, or the substrate will try to expand at different rates, resulting in a stress. For stresses due to epitaxial mismatch, the atoms of the substrate have a particular spacing due to atomic arrangement and size. The film's atoms that is deposited epitaxially will line-up with the atoms of the substrate, however if the atomic spacing of the film and the substrate do not corresponds, there will be a resulting stress.

2.2 Overview of Thin Film Deposition

There are several methods of depositing thin films onto substrates, including physical vapor deposition (PVD), chemical vapor deposition (CVD), and electroplating [17]. Chemical vapor deposition uses high temperatures that can result in high residual stresses in thin films. Physical vapor deposition, however is done at lower temperature, and therefore is less prone to create residual stresses due to mismatch in thermal coefficients [17].

2.3 Mechanics of (100) Silicon Substrate

2.3.1 Crystallographic Properties of (100) Silicon

Wafers are made from single crystal silicon, this means the atoms repeat in regular patterns on long range order throughout the material. The crystal structure of silicon is face-centered-diamond-cubic [18]. The crystal structure for silicon is shown in Figure 3. This crystal structure can be represented by taking two FCC-crystal structures and adding them together in such a manner that one of the cells is added in the same orientation as the first, but offset from the first on each axis by an amount of $x=y=z=a_0/4$ [18].

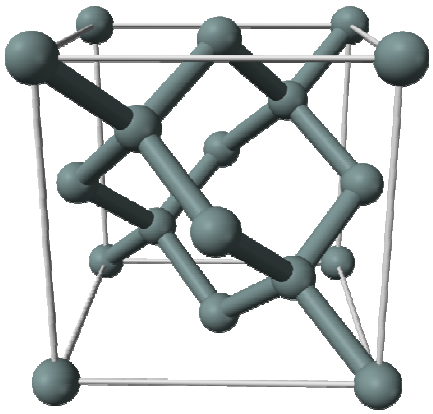

Figure 3. Crystal Structure of Silicon.

Since the silicon wafers are made from single crystal silicon, the material is anisotropic; this means the properties are different in different directions. The silicon wafers used are (100) wafers.

The orientation of the wafers is such that the (100) plane is parallel to the top surface of the wafer, and the major, or primary flat of the wafer is parallel to the (110) plane. The orientation of silicon wafers are shown in Figure 4.

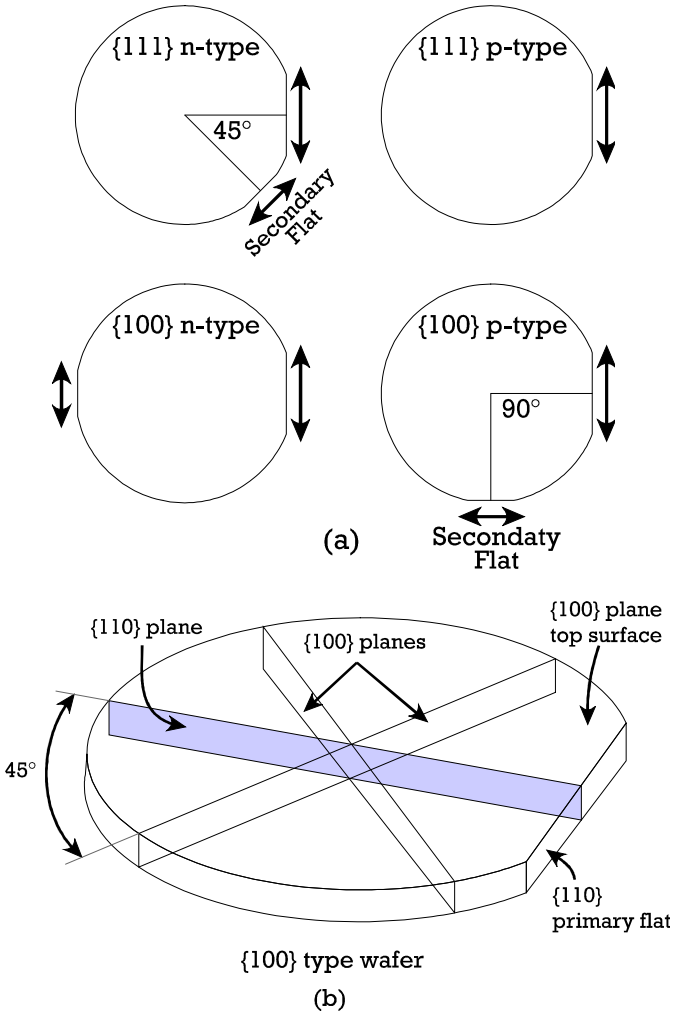

Figure 4. (a) Identifying features of single crystal silicon wafers. (b) Orientation of crystallographic planes relative to wafer features for (100) type wafer. Image courtesy of N. Maluf, An Introduction to Microelectromechanical Systems Engineering, 1st ed. Boston: Artech House, 2000.

The minor or secondary flat of the wafer is used to identify the type of wafer, depending on where the secondary flat is relative to the primary flat identifies which type of wafer it is. The secondary flat may be 45°, 90°, 180° from the primary flat, or there

may be no secondary flat on the wafer. If the wafer has no secondary flat, it a {111} p-type wafer, if the secondary flat is 45° from the primary flat it is a {111} n-type, if the secondary flat is 90° from the primary flat it is a {100} p-type, and if the secondary flat is 180° from the primary flat it is a {100} n-type silicon wafer.

2.3.2 Elastic Properties of (100) Silicon

Silicon has a cubic crystal structure, and has cubic symmetry; this means that the elastic properties can be described with only three independent properties [19]. These three independent properties can be either three elements from the stiffness matrix (i.e. C_{11}, C_{12}, C_{44}), or three elements from the compliance matrix (i.e. S_{11}, S_{12}, S_{44}) [19]. If the properties are needed for a particular direction $\hat{v}$, the values can be calculated by using equation 2.1, and 2.2 [19].

$$\frac{1}{E_{\alpha\beta\gamma}} = S_{11} - 2\left[\left(S_{11} - S_{12}\right) - \frac{1}{2}S_{44}\right]\left(l^2m^2 + m^2n^2 + l^2n^2\right) \qquad (2.1)$$

In equation 2.2 α, β, and γ are the angles between the x, y, and z axis respectively, and l, m, and n are the cosines of the angles α, β, and γ respectively [19].

$$\nu_{\alpha\beta} = \frac{S_{12} + \left(S_{11} - S_{12} - \frac{1}{2}S_{44}\right)\left(l_\alpha{}^2 l_\beta{}^2 + m_\alpha{}^2 m_\beta{}^2 + n_\alpha{}^2 n_\beta{}^2\right)}{S_{11} - 2\left(S_{11} - S_{12} - \frac{1}{2}S_{44}\right)\left(l_\alpha{}^2 m_\beta{}^2 + m_\alpha{}^2 n_\beta{}^2 + l_\alpha{}^2 n_\beta{}^2\right)} \qquad (2.2)$$

In equation 2.2, the subscripts α and β refer to the directions for the Poisson's ratio, and l, m, and n are the cosines between the x, y, and z axis and either α or β respectively. Note that the directions α and β, must be orthogonal to each other.

In the case of a deflection of a (100) Silicon wafer, the properties needed are for the directions [100], [110], and all the directions in-between. Neither the elastic modulus, nor the Poisson's ratio are constants throughout this range of directions, however the biaxial modulus in the {100}-plane is a constant [21], where the biaxial modulus is defined in equation 2.3.

$$B = \frac{E}{(1-\nu)} \qquad (2.3)$$

This biaxial modulus in the {100} plane has a value of B_{100}=179.4 GPa [20].

Chapter 3.
Stress Characterization Techniques

This chapter discusses different means of determining the stress in thin films by X-ray diffraction, curvature utilizing Stoney's equation, and other methods.

3.1 X-Ray Diffraction

This section discusses how X-ray diffraction, can be used to determine the stress in a thin film by using the $\sin^2\psi$ technique.

3.1.1 Lattice Parameter and Bragg's Law

Many materials are crystalline, that is their atoms are arranged in repeatable 3-dimensional arrays. These crystals are formed of unit cells, which contain the smallest number of atoms that repeat to form the 3-dimensional array. The unit cells can be cubic, hexagonal, or a few other types. The dimensions of these unit cells are called the lattice parameter. In the case of a cubic cell (silicon being discussed in this thesis), requires only one lattice parameter to define its dimensions. One method of determining the lattice parameter of a crystalline solid is by using Bragg's law with X-ray diffraction (XRD), to measure the interplanar spacing [22]. The interplanar spacing is the distance between two parallel planes of atoms in a crystalline material. The interplanar spacing can then be used to determine the lattice parameter. By knowing the coordinates of the diffracting plane, the intercept of the diffraction plane with the x, y, and z-axis, the lattice parameter can be determined. The correlation between the lattice parameter and the interplanar spacing is defined in equation 3.1,

$$d = \frac{a_0}{\sqrt{h^2 + k^2 + l^2}} \qquad (3.1)$$

where h, k, and l are the intercepts of the diffracting plane with the x, y, and z-axis respectively. In the case of the (100) single crystal silicon sample that was used in the experiments, h = 1, k = 0, and l = 0, therefore the lattice parameter is equal to the interplanar spacing, that is $d = a_0$.

Measuring the lattice parameter using Bragg's law involves two concepts [23]. The first concept is interference of waves. When two waves come together, having the same wavelength, and frequency, the resultant waveform is the sum of the two waves. If the two waves of the same frequency are in phase, i.e. their amplitude maxima occur at the same time, the resultant amplitude will be the sum of the two amplitudes. If they are 180° out of phase, in other words, one amplitude maxima occurs exactly midway between the amplitude maxima of the other wave, or rather the peak of one wave occurs when the other wave at its trough, when this occurs the resultant amplitude is the difference between the two amplitudes. If these two waves came from the same source, they would have the same initial amplitudes, and therefore the difference between amplitudes would be zero, that is the two waves would cancel each other out. The second concept of Bragg's Law involves simple trigonometry. When two waves hit atoms on two parallel lattice planes, one wave will travel an extra distance shown as l in Figure 5, and the same extra distance l after diffracting off of the atoms, therefore one wave will travel 2l greater distance than the other. The distance 2l that one wave travels farther than the other is a function of the distance between the two planes (shown as d in Figure 5), and the angle they make with the lattice plane. From Figure 5 it can be seen that d is the hypotenuse in a right triangle, and l is the side opposite angle θ, therefore l =

$d \sin(\theta)$. If the extra distance that one wave travels ($2l$) is exactly equal to one full wavelength (λ) or any integer multiples of λ (i.e. $n\lambda$), then the waves will be back in phase again, and there will be a constructive interference. Another way of stating this is that this is a phase shift of 360°, which brings the two amplitude maxima back in phase. Since an amplitude maxima only occurs when the phase shift is exactly equal to a multiple of wavelengths, the distance between two lattices (d) can be determined from the angle that the reflection occurs. Equation 3.2 is the Bragg's law equation.

$$d = \frac{n\lambda}{2\sin(\theta)} \qquad (3.2)$$

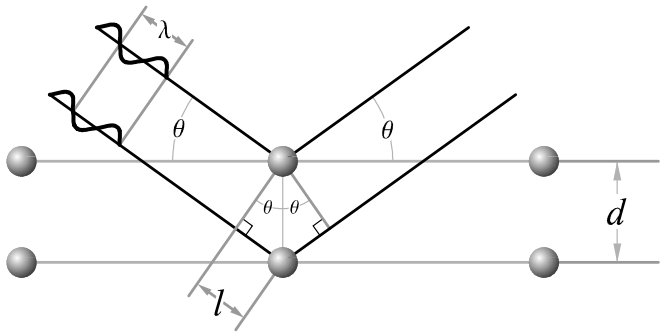

Figure 5. Determination of lattice spacing using Bragg's law.

3.1.2 Sin$^2\psi$ Technique

The sin$^2\psi$ technique is a method using X-ray diffraction, in conjunction with Bragg's law in order to determine the full strain tensor, or to determine the full stress tensor directly by applying Hook's law [24-26]. The full strain, and also the full stress tensor contains six components, therefore a minimum of six measurements are needed, however more measurements are often taken in order to reduce the amount of uncertainty [26,27].

The $\sin^2\psi$ technique requires a coordinate system to be established, that is the x, y, and z-directions need to be assigned, although these directions may be assigned using any orientation, a standard orientation to the coordinate system is usually used. This standard orientation usually consists of the x, and y-axis being in the plane of the sample surface, and therefore the z-axis is the direction normal to the surface. Only two angles need to be given in order to establish a unique direction, the angles that are used to define a direction are ϕ, and ψ. The ϕ-angle is the angle between the x-axis, and the projection of a vector-$\hat{v}$, onto the xy-plane. The ψ–angle, also known as the tilt angle, is the angle between the z-axis, and the vector, as shown in Figure 6. The angle-θ mentioned in the previous section is the angle at which the X-rays impinge on the plane of atoms, when Bragg's law is satisfied in order to create a reflection.

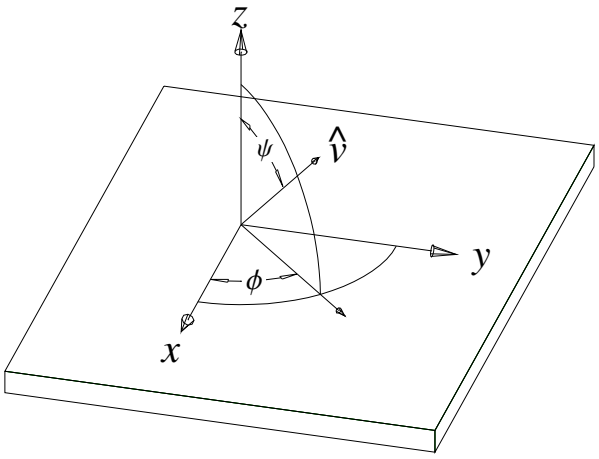

Figure 6. Coordinate System Used for the $\sin^2\psi$ Technique.

Before giving a detailed explanation of the $\sin^2\psi$ technique, a simple basis of how the ψ-angle, or rather the tilt angle plays a role in determining the strain tensor, which is used to calculate the stress tensor [28]. This simple basis is as follows.

First consider a lattice that is under tensile stress, and is parallel to the applied stress. This stress will result in a strain that elongates the lattice parameter. Second consider a lattice that is under tension, but this lattice is perpendicular to the applied stress. This lattice parameter will be reduced due to the Poisson's ratio. Those lattice parameters that are at some angle other than parallel, or perpendicular to the applied stress, will experience an amount of elongation due to the component which is parallel, and some reduction due to the component that is perpendicular, as shown in Figure 7.

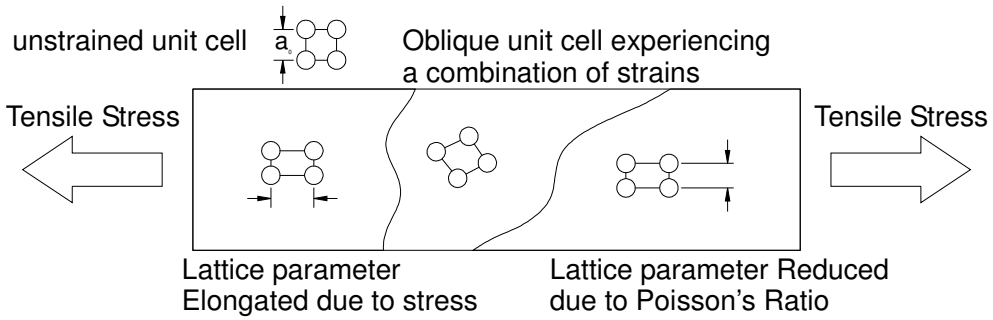

Figure 7. Basic principles of $\sin^2\psi$ stress determination.

This explanation is used only to give a basic idea as to how the ψ-angle plays a role in determining the full strain tensor, a much more complete explanation is needed to understand the $\sin^2\psi$ technique.

3.1.3 Strain Transformation

In order to calculate the stress using the $\sin^2\psi$ method the first thing needed is to find the 3-dimensional strain projection, that is it is needed to determine what the strain will be along a particular direction, given the strains for a given coordinate system. The

basis for this strain transformation is that each of the strains from the original coordinates is projected onto the new axis [29,30]. The 2D-strain Transformation is a superposition of each of the individual strain components; this means that each of the strain components can be added separately. The transformation done here is a 3D-strain transformation, as opposed to a 2D-strain transformation. This requires two transformations for each component to project each component onto the new axis instead of just one transformation. In addition the 3D strain transformation has six components of strain, whereas a 2D strain transformation has only three components.

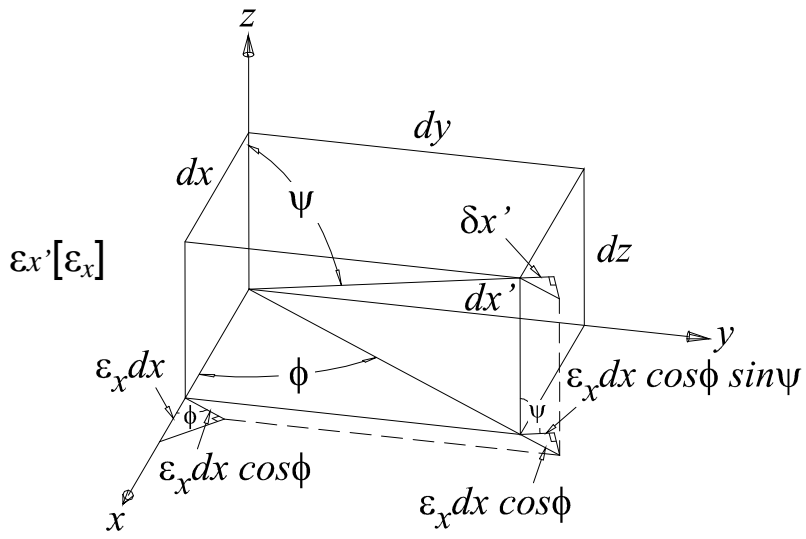

Figure 8. ε_x Component of the 3D-Strain Transformation to the $\varepsilon_{x'}$ Axis.

As shown in Figure 8, ε_x is multiplied by dx to give the displacement $\varepsilon_x dx$. This displacement is projected onto the 'ϕ-axis,' which gives $\varepsilon_x dx \cos\phi$. This is projected onto the x'-axis, which gives $\varepsilon_x dx \cos\phi \sin\psi$. The definition of the strain along the new axis is equation 3.3, where equation 3.4 is determined from trigonometry and solving for dx' in

terms of dx gives equation 3.4. Equation 3.5 can be plugged into equation 3.3 to give equation 3.6, which is the strain component along the new axis.

$$\varepsilon_x' = \delta x' / dx' \qquad (3.3)$$

$$dx = dx' \sin\psi \cos\phi \qquad (3.4)$$

$$dx' = dx/(\sin\psi \cos\phi) \qquad (3.5)$$

$$\varepsilon_{x'}[\varepsilon_x] = \frac{\delta x'}{dx'} = \frac{\varepsilon_x dx \cdot \cos\phi \cdot \sin\psi}{\frac{dx}{\cos\phi \sin\psi}} = \varepsilon_x \cos^2\phi \cdot \sin^2\psi \qquad (3.6)$$

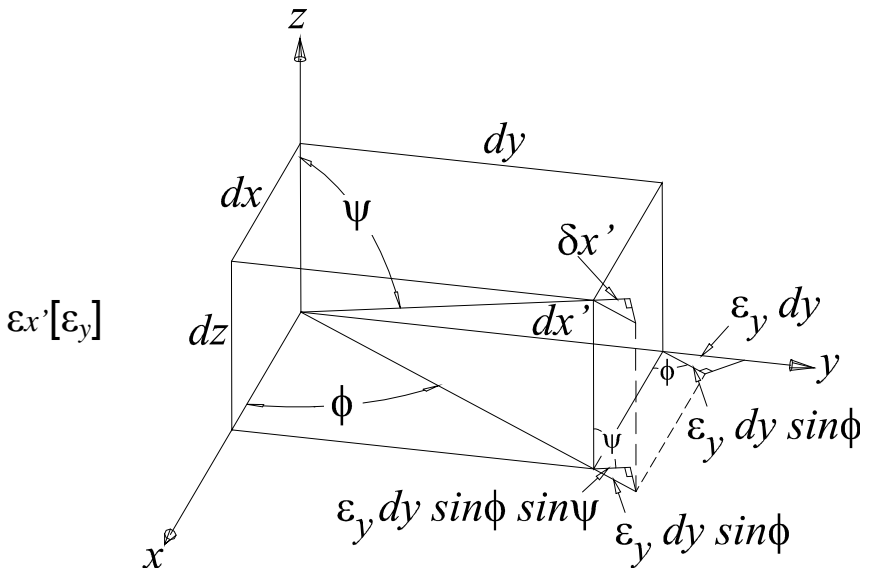

Figure 9. ε_y Component of the 3D-Strain Transformation to the $\varepsilon_{x'}$ Axis.

As shown in Figure 9, ε_y is multiplied by dy to give the displacement $\varepsilon_y dy$. This displacement is projected onto the 'ϕ-axis,' this gives $\varepsilon_x\ dy\ \sin\phi$. Equation 3.7 is determined from trigonometry and solving for dx' in terms of dy gives equation 3.8.

Equation 3.8 can be plugged into equation 3.3 to give the strain component along the new axis

$$dy = dx' \sin\psi \sin\phi \qquad (3.7)$$

$$dx' = dy/(\sin\psi \sin\phi) \qquad (3.8)$$

$$\varepsilon_{x'}[\varepsilon_y] = \frac{\delta x'}{dx'} = \frac{\varepsilon_y dy \cdot \sin\phi \cdot \sin\psi}{\frac{dy}{\sin\phi \sin\psi}} = \varepsilon_y \sin^2\phi \cdot \sin^2\psi \qquad (3.9)$$

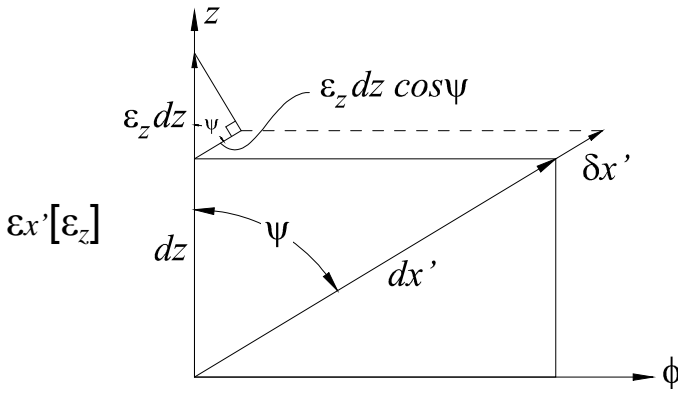

Figure 10. ε_z Component of the 3D-Strain Transformation to the $\varepsilon_{x'}$-Axis.

This component of the strain is independent of angle-ϕ, and therefore can be illustrated using a two-dimensional figure along the 'ϕ-axis' and the z-axis, as shown in Figure 10. ε_z is multiplied by dz to give the displacement $\varepsilon_z\, dz$. Equation 3.10 is determined from trigonometry and solving for dx' in terms of dz gives equation 3.11. Equation 3.11 can be plugged into equation 3.3 to give equation 3.12, which is the strain component along the new axis.

$$dz = dx' \cos\psi \qquad (3.10)$$

$$dx' = dz/\cos\psi \qquad (3.11)$$

$$\varepsilon_{x'}[\varepsilon_z] = \frac{\delta x'}{dx'} = \frac{\varepsilon_z dz \cdot \cos\psi}{\frac{dz}{\cos\psi}} = \varepsilon_z \cos^2\psi \qquad (3.12)$$

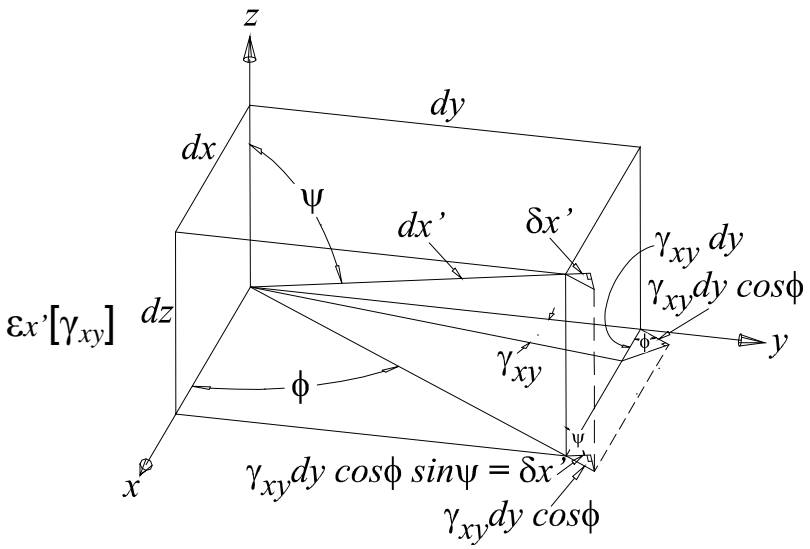

Figure 11. γ_{xz} Component of the 3D-Strain Transformation to the $\varepsilon_{x'}$-Axis.

As shown in Figure 11, γ_{xy} is multiplied by dy to give the displacement $\gamma_{xy}dy$. This displacement is projected onto the 'ϕ-axis,' this gives $\gamma_{xy}dy\cos\phi$. Next, this is projected onto the x'-axis, which gives $\gamma_{xy}dy\cos\phi\sin\psi$. The definition of the strain along the new axis is equation 3.3, where equation 3.7 is determined from trigonometry and solving for dx' in terms of dy gives equation 3.8. Equation 3.8 can be plugged into equation 3.3 to give equation 3.13, which is the strain component along the new axis.

$$\varepsilon_{x'}[\gamma_{xy}] = \frac{\delta x'}{dx'} = \frac{\gamma_{xy} dy \cdot \cos\phi \cdot \sin\psi}{\frac{dy}{\sin\phi \sin\psi}} = \gamma_{xy} \sin(2\phi) \cdot \sin^2\psi \qquad (3.13)$$

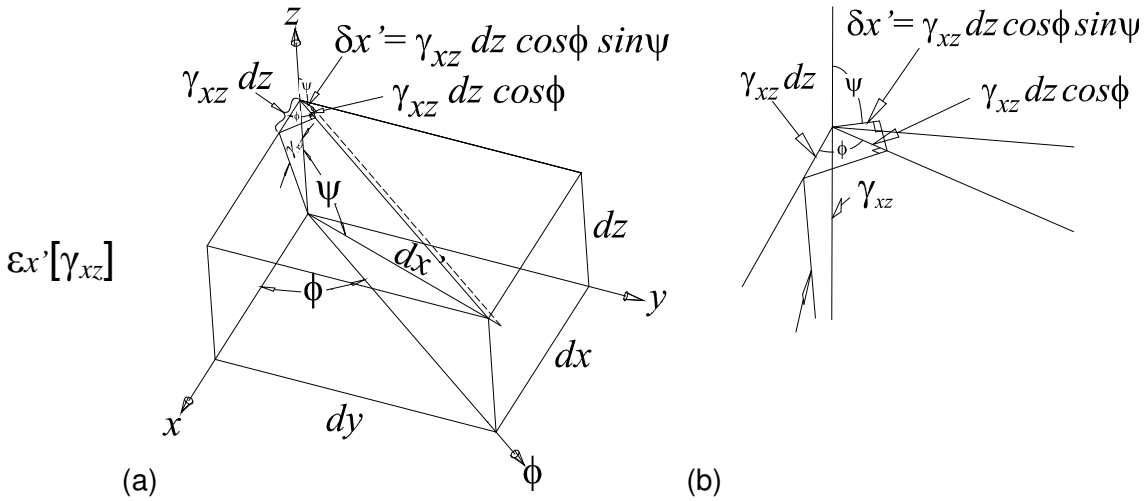

Figure 12. (a) γ_{xz} Component of the 3D-Strain Transformation to the $\varepsilon_{x'}$-Axis.

(b) Close-Up of the Strain Transformation Components.

As shown in Figure 12, γ_{xz} is multiplied by dz to give the displacement $\gamma_{xy} dz$. This displacement is projected onto the 'ϕ-axis,' this gives $\gamma_{xz} dz \cos\phi$. Next, this is projected onto the x'-axis, which gives $\gamma_{xz} dz \cos\phi\sin\psi$. The definition of the strain along the new axis is equation 3.3, where equation 3.10 is determined from trigonometry and solving for dx' in terms of dz gives equation 3.11. Equation 3.11 can be plugged into equation 3.3 to give equation 3.14, which is the strain component along the new axis.

$$\varepsilon_{x'}[\gamma_{xz}] = \frac{\delta x'}{dx'} = \frac{\gamma_{xz} dz \cdot \cos\phi \cdot \sin\psi}{\frac{dz}{\cos\psi}} = \gamma_{xz} \cos\phi \cdot \sin(2\psi) \qquad (3.14)$$

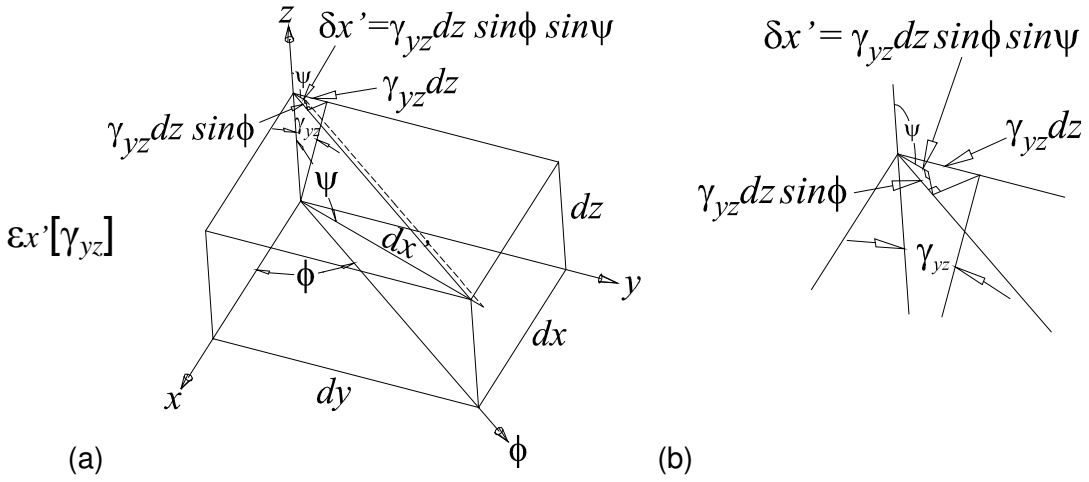

Figure 13. (a) γ_{yz} Component of the 3D-Strain Transformation to the $\varepsilon_{x'}$-Axis.

(b) Close-Up of the Strain Components.

As shown in Figure 13, γ_{yz} is multiplied by dz to give the displacement $\gamma_{yz} dz$. This displacement is projected onto the 'ϕ-axis,' this gives $\gamma_{yz}\, dz \sin\phi$. This is projected onto the x'-axis, which gives $\gamma_{yz} dy \sin\phi \sin\psi$. The definition of the strain along the new axis is equation 3.3, where equation 3.10 is determined from trigonometry and solving for dx' in terms of dz gives equation 3.11. Equation 3.15 is the γ_{yz} strain component, along the new axis.

$$\varepsilon_{x'}[\gamma_{yz}] = \frac{\delta x'}{dx'} = \frac{\gamma_{yz} dz \cdot \sin\phi \cdot \sin\psi}{\frac{dz}{\cos\psi}} = \gamma_{yz} \sin\phi \cdot \cos\psi \cdot \sin\psi \tag{3.15}$$

By adding all the individual strain transformation components together, yields equation 3.16, which is the 3-dimensional strain transformation.

$$\begin{aligned}\varepsilon_{x'} &= \varepsilon_x \cos^2\phi \sin^2\psi + \varepsilon_y \sin^2\phi \sin^2\psi + \varepsilon_z \cos^2\psi \\ &+ \gamma_{xy} \sin 2\phi \sin^2\psi + \gamma_{xz} \cos\phi \sin 2\psi + \gamma_{yz} \sin\phi \sin 2\psi\end{aligned} \tag{3.16}$$

3.1.4 Sin$^2\psi$ Equation

Equation 3.16 can be changed to an equation of stress by utilizing the generalized form of Hook's Law. Also by using the fact that $\sin^2\psi = 1 - \cos^2\psi$, the terms may be grouped to form equation 3.17 [31].

$$\begin{aligned}\varepsilon_{\phi\psi} = \frac{d_{\phi\psi} - d_0}{d_0} &= \frac{1+\nu}{E}(\sigma_x \cos^2\phi + \sigma_y \sin^2\phi + \tau_{xy} \sin 2\phi - \sigma_z)\sin^2\psi + \\ &\frac{1+\nu}{E}\sigma_z - \frac{2\nu}{E}(\sigma_x + \sigma_y + \sigma_z) + \frac{1+\nu}{E}(\tau_{xz}\cos\phi + \tau_{yz}\sin\phi)\sin 2\psi\end{aligned} \tag{3.17},$$

where E is the elastic modulus of the film, ν is Poisson's ratio of the film, and d_0 is the unstrained lattice parameter. The equation for the stress along the ϕ-direction is defined in equation 3.18.

$$\sigma_\phi = \sigma_x \cos^2\phi + \sigma_y \sin^2\phi + \tau_{xy} \sin 2\phi \tag{3.18}$$

Since this stress is in a thin film, and therefore near the surface, the normal stress in the z-direction will not exist. By substituting equation 3.18 into equation 3.17, one derives:

$$\varepsilon_{\phi\psi} = \frac{d_{\phi\psi} - d_0}{d_0} = \frac{1+\nu}{E}\sigma_\phi \sin^2\psi - \frac{2\nu}{E}(\sigma_x + \sigma_y) + \frac{1+\nu}{E}(\tau_{xz}\cos\phi + \tau_{yz}\sin\phi)\sin 2\psi \quad (3.19)$$

If a plot is made with $d_{\phi\psi}$ vs. $\sin^2\psi$, there will be three types of behavior, linear behavior, ψ–splitting behavior, and oscillatory behavior [24], as shown in Figure 14.

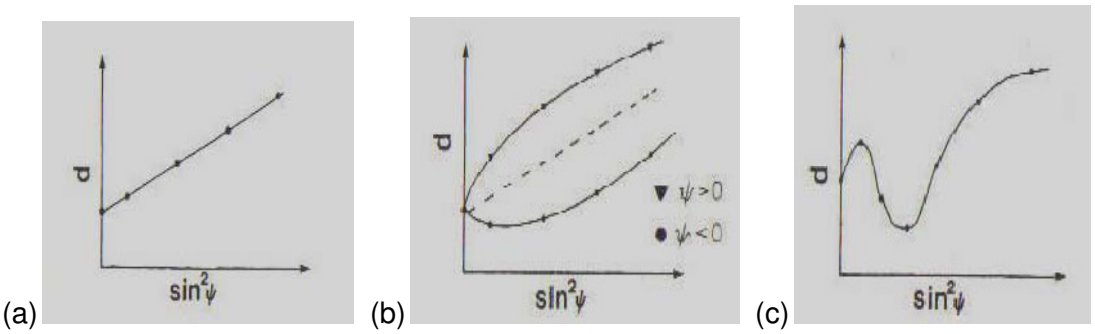

Figure 14. $d_{\phi\psi}$ vs. $\text{Sin}^2\psi$ for (a) Linear Behavior, (b) ψ-Splitting Behavior, and (c) Oscillatory Behavior. Adapted from [24].

If shear stresses τ_{xz}, and τ_{yz} are zero, equation 2.13 will have a linear behavior with $\sin^2\psi$. If the shear stresses are non-zero, the plot of $d_{\phi\psi}$ vs. $\sin^2\psi$ will have a ψ–splitting behavior. If the plot of $d_{\phi\psi}$ vs. $\sin^2\psi$ shows an oscillatory behavior it indicates that the material is textured and strain cannot be solved using equations mentioned above [24]. The methods of determining the stress in the material using the first two types of behavior are discussed in the next section.

3.1.5 Calculation of Stress Using $\mathrm{Sin}^2\psi$

As mentioned in the previous section, a plot of $d_{\phi\psi}$ vs. $\sin^2\psi$ will have three different types of behavior, linear, ψ-splitting, and oscillatory behavior, shown in Figure 14.

If the plot is linear, this means that the two shear terms, τ_{xz}, and τ_{yz} are zero; therefore equation 3.19 is reduced to equation 3.20.

$$\varepsilon_{\phi\psi} = \frac{d_{\phi\psi} - d_0}{d_0} = \frac{1+\nu}{E}\sigma_\phi \sin^2\psi - \frac{2\nu}{E}(\sigma_x + \sigma_y) \qquad (3.20)$$

Differentiating equation 3.20 with respect to $\sin^2\psi$, results in equation 3.21.

$$\frac{\partial d_{\phi\psi}}{\partial(\sin^2\psi)}\frac{1}{d_0} = \frac{1+\nu}{E}\sigma_\phi \qquad (3.21)$$

Using equation 3.21, and simply solving for σ_ϕ, one gets equation 3.22:

$$\sigma_\phi = \left(\frac{E_f}{1+\nu_f}\right)\frac{1}{d_0}\left(\frac{\partial d_{\phi\psi}}{\partial \sin^2\psi}\right) \qquad (3.22)$$

Equation 3.22 illustrates that the stress should be proportional to the slope of the $d_{\phi\psi}$ vs. $\sin^2\psi$ plot. It would only be necessary to take measurements at two ψ–tilts in order to determine the slope; however more points are usually taken in order to reduce the amount of uncertainty [50]. As seen in Figure 15, the $d_{\phi\psi}$ vs. $\mathrm{Sin}^2\psi$ plot, the behavior is not exactly linear, probably either due to a small amount of shear stress, or due to some uncertainty in the measurements.

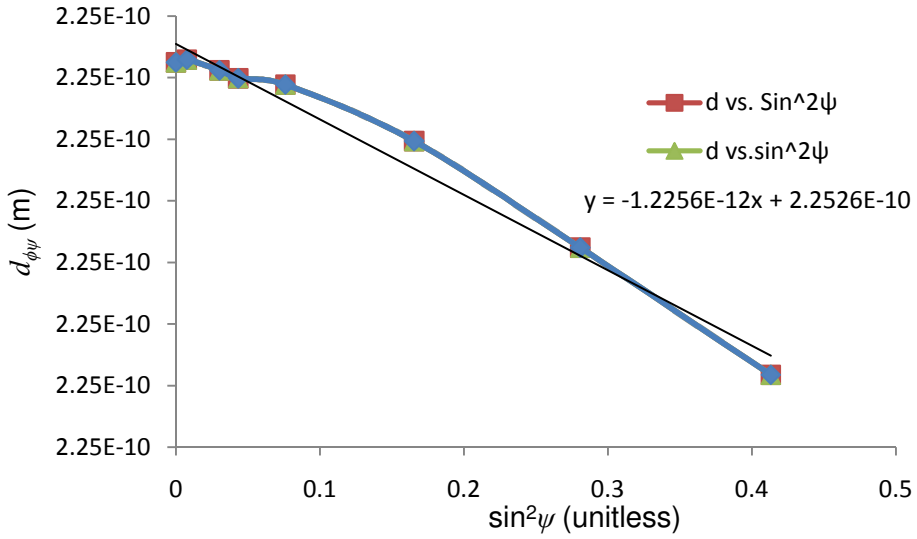

Figure 15. Example of a $d_{\phi\psi}$ vs. $\text{Sin}^2\psi$ Plot for Tungsten Film.

The slope is found by doing a linear regression of the data. In this case the material is Tungsten, the slope of the plot is -1.2256x10^{-12} m, d_0 is 2.2524x10^{-10} m, E is 300 GPa, and ν is 0.3, therefore in this example the stress along the ϕ–axis is 1.26 GPa compressive, because the slope is negative. However, in order to calculate the full stress tensor, additional values are needed. To do this similar plots are taken at different ϕ-angles. Examining equation 3.18, if ϕ is set to 0°, then $\sin^2\phi = 0$, $\sin(2\phi) = 0$, and $\cos^2\phi = 1$. As a result equation 3.18 reduces to σ_x. If the angle ϕ is set to 90°, then in equation 3.18, $\sin^2\phi = 1$, $\sin(2\phi) = 0$, and $\cos^2\phi = 0$, and equation 2.4 is reduced to σ_y. Finally if ϕ is set to 45°, then $\sin^2\phi = 0.5$, $\cos^2\phi = 0.5$, and $\sin(2\phi) = 1$, and equation 3.18 is reduced to $0.5\sigma_x + 0.5\sigma_y + \tau_{xy}$. Since σ_x, and σ_y are known, τ_{xy} can be solved for. Any three different angles for ϕ can be used; however choosing the above values greatly simplifies calculations.

If the plot shows ψ–splitting behavior, the above method can be used, however in order to find the slope of $d_{\phi\psi}$ vs. $\sin^2\psi$, an average between the slopes for positive, and negative ψ–tilts needs to be used. In equation 3.22 the component $\partial d_{\phi\psi}/\partial \sin^2\psi$ is determined by doing a linear regression of the $d_{\phi\psi}$, vs. $\sin^2\psi$ data, as mentioned in the next section.

3.1.6 $\mathrm{Sin}^2\psi$ Example

Table-1 is an example of data of diffraction reflections that was taken from a tungsten film on a (100) silicon wafer, at various ψ-tilts at the Technical University of Dresden.

Table 1. $\mathrm{Sin}^2\psi$ Data for Tungsten Film on a (100) Silicon Wafer.

ψ (deg)	2θ(Pseudo Voigt)	$d_{\phi\psi}$	$\sin^2\psi$
-40	40.1769	2.24182E-10	0.413175911
-24	40.1871	2.24128E-10	0.165434697
-10	40.1659	2.24241E-10	0.03015369
0	40.1707	2.24216E-10	0
5	40.1715	2.24211E-10	0.007596123
10	40.1670	2.24235E-10	0.03015369
12	40.1659	2.24241E-10	0.043227271
16	40.1623	2.2426E-10	0.075975952
24	40.1661	2.2424E-10	0.165434697
32	40.1716	2.24211E-10	0.280814427
40	40.1757	2.24189E-10	0.413175911

To calculate the slope of d vs. $\sin^2\psi$ one would take the average slope of negative psi tilts and positive psi tilts. To calculate the slope for negative psi tilts a linear regression of all the negative psi tilts are taken, where $d_{\phi\psi}$ is the y-axis, and $\sin^2\psi$ is the x-axis. Similarly a linear regression is taken for all the positive psi tilts using the same manner that was done for the negative psi tilts. An average of the negative and positive slopes is then used in the calculations [50]. The values, including the elastic properties,

and the slopes for the negative, and positive, as well as the average slope are given in table 2. In order to find the full stress tensor the same procedure will be done for two other ϕ-angles.

Table 2. Mechanical Properties of Tungsten.

E=	3.00E+11 Pa
ν=	0.3
E/(1+ ν)=	2.30769E+11 Pa
slope[neg]=	8.51906E-13
slope[pos]=	-5.63543E-13
slope[ave]=	1.44182E-13
d[110]=a[0]/sqrt(2) =	2.238134E-10
σ =	148.6625 MPa Tensile

3.2 Curvature Methods

3.2.1 Stoney's Equation

Stoney's equation is used to determine the stress in a thin film from the amount of curvature in the wafer. This formula is based on simple beam bending formulas, where the tension and compressive forces act on the cross-section to create a moment at the cross-section resulting in the curvature, as shown in Figure 16.

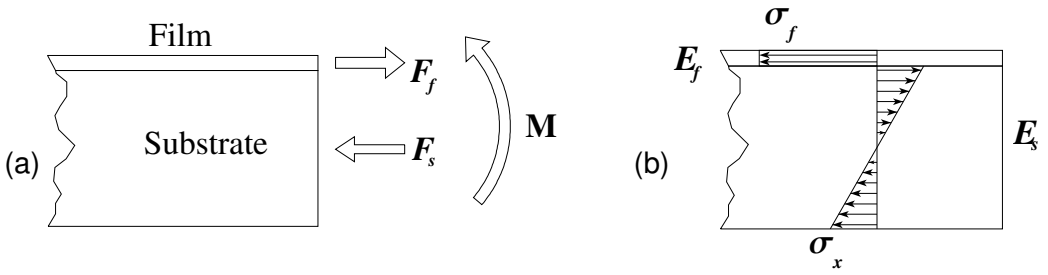

Figure 16. Forces Acting on a Cross-Sectional Area Act as the Basis of Stoney's Equation.

Equation 3.23 is Stoney's equation [32]. Stoney's equation can also be written using variables for curvature κ, or $\Delta\kappa$, which is the reciprocal of the radius of curvature.

$$\sigma_r = \frac{E_s}{6(1-\nu_s)}\frac{h_s^2}{h_f}\left(\frac{1}{R_2}-\frac{1}{R_1}\right) \qquad (3.23)$$

The variables used in Stoney's equation are: E_s - elastic modulus of the substrate, ν_s - Poisson's ratio of the substrate, h – film thickness, where subscripts s, and f refer to substrate, and film respectively, R - radius of curvature of the substrate, where subscript-1 refers to the radius of curvature before deposition and subscript-2 refers to the radius of curvature after deposition [29].

3.2.2 Curvature Measuring Techniques

The key to using Stoney's equation is to be able to determine substrate curvature with a sufficient enough accuracy. There are several methods to determining the curvature, including IONIC stress-gauge, profilometer, and X-ray diffraction.

The IONIC stress-gauge determines the curvature of the wafer at a single point, in the center by determining the height of the center, relative to a fixed height.

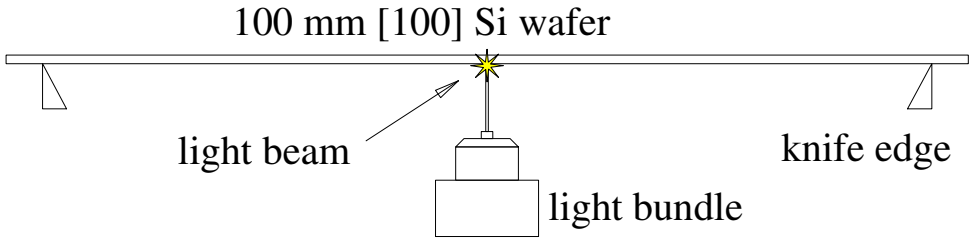

Figure 17. IONIC Stress-Gauge Measurement.

The IONIC stress-gauge uses the reflection of light from a fiber bundle in order to determine the curvature as shown in Figure 17. In this manner, the IONIC stress-gauge

does not touch the surface of the wafer, thereby reducing any damage to the wafer due to contact.

Some of the key features of the IONIC stress-gauge setup are the knife edge, which has a very thin contact area. This knife edge has a very small surface area in contact with the wafer, which helps ensure that the possibility of errors due to debris between the wafer, and the contact surface is very low. The knife edge is also very near the outer edge, this means that the radius is determined over the largest possible distance, to minimize the amount of uncertainty. One of the advantages in the IONIC stress-gauge is the simplicity of the setup. Some of the disadvantages of the IONIC stress-gauge are that it only determines the deflection at a single point. In fact the curvature can vary over the entire wafer [33,34]. Another disadvantage is that the IONIC stress-gauge is very sensitive, and any deviation of the reflectivity on the back surface of the wafer can cause very large inaccuracies.

A profilometer measures the wafer height at several points, in this manner changes in curvature can be calculated over the surface of the wafer. This device uses a stylus to scan from one side of the wafer to the other, recording the scan height. Profilometers can have a resolution approximately to that of an atomic spacing, and therefore can accurately determine the radius of curvature. One disadvantage to profilometers is the data is scattered [35] that is it shows abrupt changes in height over a very small distance. Because of this data scatter, data smoothing techniques must be used [36]. There are different types of data smoothing, one type of data smoothing is to fit the data to a polynomial [37]. If the polynomial is a second order polynomial, the curvature will be constant, if small deflection formulas are used.

X-ray diffraction can also be used to determine curvature profile [38]. The curvature determination is done by utilizing a rocking curve scan on single crystal films.

The rocking curve scan is where the emitter and collector move in sync with each other, this is similar to having the wafer tilt as the emitter and collector remain stationary. When a reflection occurs during a rocking scan, the normal to the wafer is the bisection of the angle between the emitter and collector. By taking readings at several points, the curvature can be determined [38].

Chapter 4.
In-Situ Bending Experiments in XRD

An experiment was done at Technical University (TU) in Dresden Germany in order to demonstrate the ability to determine the distortion in a (100) silicon wafer. The experiment consisted of using a piece of a (100) silicon wafer in a four-point bending setup that was deformed to a certain amount and then the stress was determined [39]. The stress was determined by first measuring the lattice parameter, and comparing it to a known unstressed lattice parameter. Then the stress was calculated by using the elastic constants of the material.

4.1 Four-Point Bending Apparatus Design

In order to perform the following measurements a four point bending fixture needed to be designed and built, as shown schematically in Figure 18.

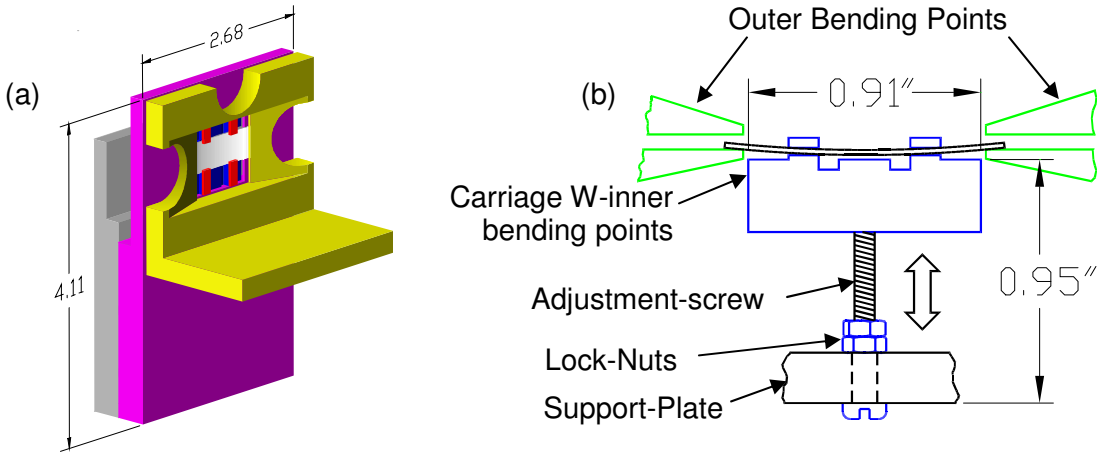

Figure 18. (a) 4-Point Bending Fixture. (b) Description of Parts.

The four point bending fixture was designed by the author, and built by machinists at TU-Dresden. The reason for using a four point bending fixture, as opposed to a three point bending fixture is that a four point bending fixture will have a constant radius of curvature between the inner bending points [40,41], as shown in Figure 19.

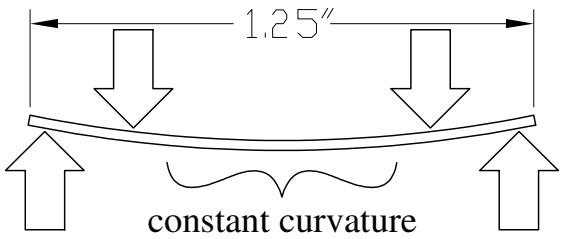

Figure 19. Constant Radius of Curvature Between Inner Bending Points on a 4-Point Bending Setup.

The stress between the inner points is constant. This will help eliminate errors caused by stress being a function of the x-direction, should the x-ray not hit the exact same spot on the (100) silicon wafer. The bending fixture consists of a threaded carriage providing the inner points for bending. A screw is fitted to the carriage to provide the motion; this same screw goes through an adjustment plate to provide the force on the carriage. The carriage is also fitted with support tabs. These tabs provide the inner bending points in order to put the bottom of the wafer into tension. The parts for the bending fixture are shown in Figure 18b. The entire assembly is attached to the x-ray diffraction machine by means of elongated holes to provide adjustment. The setup once installed was tested to be level by use of a common carpenter's level, and should it have needed leveling shims perpendicular to the machine would have been used.

4.2 System Alignments

After the setup was properly installed several alignment tests were performed. These adjustments included vertical alignment, basic level alignment, and a rocking scan to more precisely level the setup.

4.2.1 Vertical Alignment

The test for vertical alignment consisted of performing a scan so that the emitter, and collector are directly facing each other initially. This setup is shown in Figure 20.

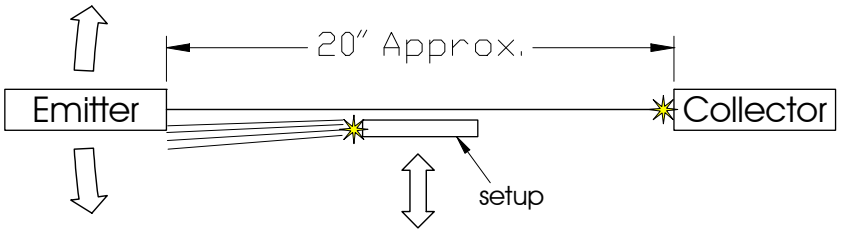

Figure 20. Alignment Test for Vertical Position.

It should be noted that in doing this test it is important to insert a copper shield in either the emitter, or collector aperture, in order to reduce the intensity of the X-rays that will be hitting the collector. This scan is done with the collector remaining stationary at the 180°-mark during the scan. The emitter is initially below the 0°-mark, in other words the emitter is situated so that the X-rays are impinging on the wafer, or the bending fixture. The emitter continues the scan moving upward, to a point that is both past the 0°-mark, and past a point where the X-rays pass over the wafer, and are detected by the collector. After the scan is done, the angle at which the collector first started to absorb the X-rays is observed. If the angle where the collector first absorbed the X-rays is lower

than the 0°-mark, it indicates that the fixture is too low, and therefore needs to be raised, as shown in Figure 21.

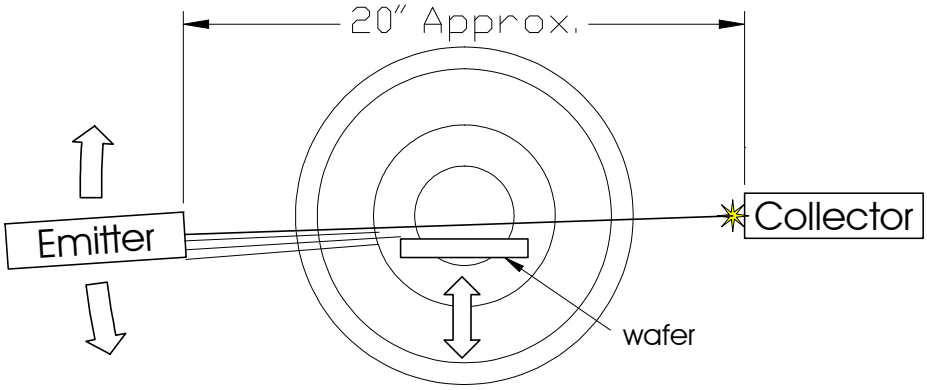

Figure 21. Illustration of an Alignment Test, with the Wafer Too Low.

If on the other hand the angle where the collector first started to absorb X-rays is above the 0°-mark, it indicates that the fixture is too high, and needs to be lowered, as shown in Figure 22. This type of scan is repeated until the angle where the collector first starts to absorb X-rays is within small tolerance from the 0°-mark. At each point that the fixture was adjusted, it was checked for level.

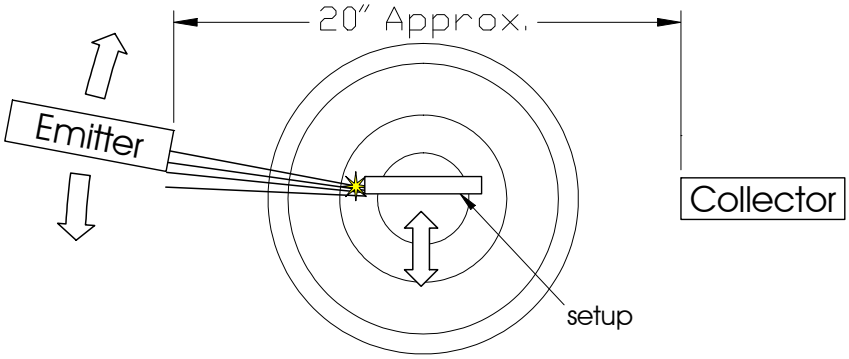

Figure 22. Illustration of an Alignment Test with the Wafer Too High.

4.2.2 Zeroing the Sample

The first scan performed on the sample was done with no stress on the wafer in order to determine the unstrained lattice spacing of the sample. It was necessary to locate the point where there would be no slack between the sample, and the setup, nor any initial stress in the sample. The sample was adjusted in order to produce a minimal amount of play between the sample, and the setup, or a minimal amount of initial stress.

This was done by initially adjusting the screw so that there is slack between the sample, and the setup, then the screw is adjusted slightly, and then the sample is checked for play. In order to check for play, a piece of paper is used to attempt to move the sample in the fixture, if the sample moves, there is still play in the setup, and the screw is turned an additional amount. This is repeated until the sample is not able to be moved by the piece of paper.

This process has a certain amount of resolution, the resolution in this case means that there is an amount that the screw is turned between each time that the sample is checked for slack. The result of this is that the point where the slack in the sample is taken up is anywhere in between two points where the sample is checked. In order to produce a finer resolution the process is done twice, the first time with the screw being turned a fairly large amount in-between each check, in order to get an approximate location of the zero point. The zeroing process is repeated a second time, this time where the zero point is known to within a certain amount, and much finer turns of the screw being made between each time the sample is checked. In order to prevent a hysteresis error, the screw was only turned in one direction between checking the sample.

4.2.3 Rocking Scan

To perform the rocking-scan on the setup, a regular 2θ-scan was performed first. Leveling of the initial setup was performed to be able to determine a reflection during the 2θ-scan. If a reflection cannot be determined at this point, it would indicate that the setup was not properly aligned. If a reflection occurs during the 2θ-scan, then a rocking scan can be done in order to make a much more accurate alignment of the setup. The reflection that occurs during the initial 2θ-scan will more than likely have a much lower intensity, than a reflection should be for a single crystal reflection, which is an indication that the wafer is not properly aligned to an accurate enough degree, as shown in Figure 23.

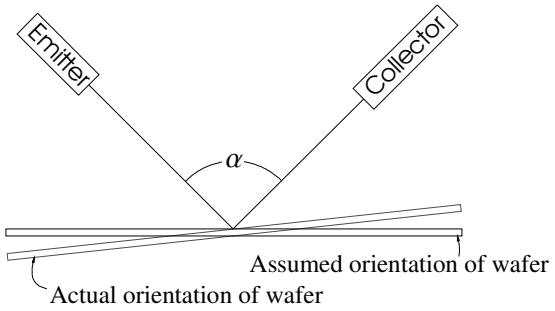

Figure 23. The 2θ-Scan with a Misaligned Wafer.

The reason for having a lower intensity is because the diffracted X-rays have the highest intensity at the true diffraction angle, and greatly diminish at angles other than the true diffracted angle as shown in Figure 24.

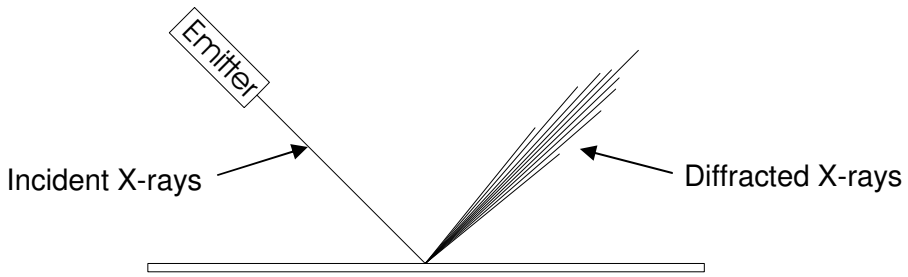

Figure 24. Relative Intensity of Diffracted X-Rays.

First the 2θ-angle at which the reflection occurred is recorded, and the rocking scan is done so that there is a fixed angle between the emitter and collector as the scan is done, this is shown in Figure 25. Doing a rocking scan in this manner has the same effect as if the setup were to be rotated about a point where the centerline of the emitter and collector intersect. The rocking scan however can be done in a much more accurate manner, and it will rotate about a constant point.

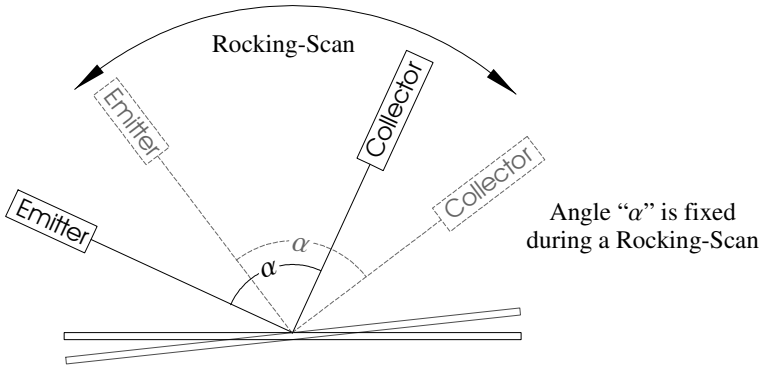

Figure 25. Rocking-Scan Used to Determine the Alignment of the Wafer.

After the rocking scan is done the angle at which a reflection occurs is recorded, this will be used as the offset angle in the next step. The next step is to do a 2θ-offset-scan. The angle where the reflection occurred during the rocking scan is used as the

offset angle for the 2θ-offset-scan. If the misalignment in the initial setup is large enough, it will produce a significant error when doing the rocking-scan. If this happens it may require several iterations of rocking-scans, followed by 2θ-offset-scans in order to reduce the error caused by misalignment. The 2θ-offset-scan is similar to the 2θ-scan, with the exception that instead of the emitter and collector scanning at equal angles from the 90°-mark, the emitter and collector are scanned at equal angles from a point that is offset from 90°-mark, hence the term 2θ-offset-scan. An illustration of the 2-offset-scan is shown in Figure 26.

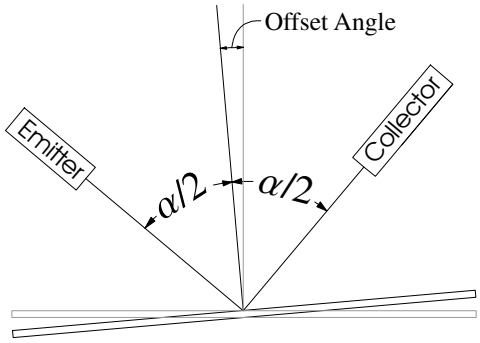

Figure 26. Using an Offset Angle to Correct for Angular Alignment.

4.3 Sources of Error

There are several sources of error, or uncertainty in the measurements, these sources include alignment, peak determination, and the bending fixture. The alignment can cause errors due to the detector not picking up the true diffracted X-rays. Even if the setup is exactly aligned, there is an amount of uncertainty in locating the diffraction peaks. The bending fixture caused errors due to changing the height of the wafer.

4.3.1 Errors Due to Change in Height

The bending fixture mentioned previously deflected the wafer by changing the height of the inner bending points; as a result this caused a change in the height of the wafer, at the point where measurements were taken, by an amount greater than the amount of adjustment of the carriage as shown in Figure 27. This was done partially due to a lack of foresight on the part of the author; however given the time frame of the experiment, and the amount of engineering needed, the method used was the most practical means in order to carry out the experiments given the time frame, and so as to not place too heavily a burden on the machinists at TU-Dresden. The errors that were produced as a result of the changing height of the wafer sample needed to be addressed.

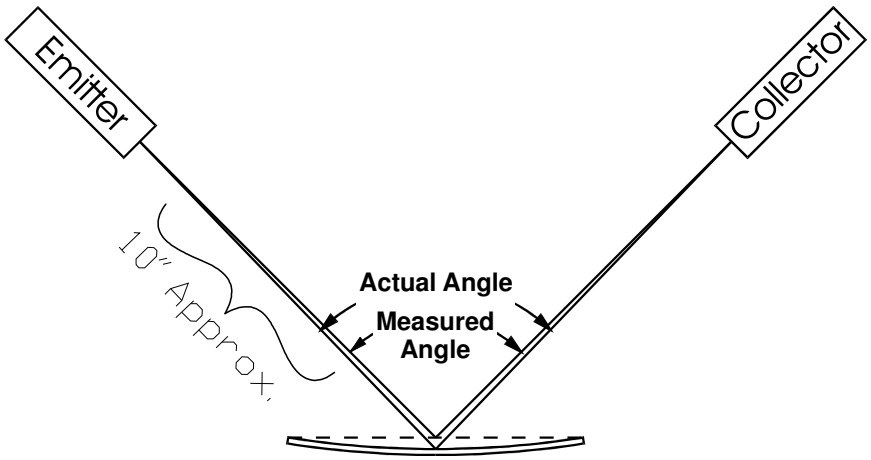

Figure 27. Source of Error Due to Changing Height of Wafer Sample.

4.4 Depth of X-Ray Penetration

4.4.1 Basis of X-Ray Absorption

Materials absorb X-rays as the X-rays pass through them, the amount of X-rays that are absorbed depends on several factors. The main factors that determine the intensity of the resulting beam as it passes through a material are the depth of the material that the X-rays have passed through, and the material properties [42]. As a result the intensity of the X-rays after it has passed through a certain length of a material is according to equation 4.1 [42,43],

$$I = I_0 e^{-\mu \cdot x} \quad \text{or} \quad I = I_0 e^{-(\mu/\rho)\cdot\rho\cdot x} \qquad (4.1)$$

where I refers to the intensity of the beam at depth x, I_0 is the original intensity of the beam, ρ is the density of the material, and μ is the mass attenuation coefficient. This equation follows the same principles for absorption of optical rays, known as Beer-Lambert's law.

4.4.2 Depth of Attenuation

According to equation 1.1, the depth that the X-ray will penetrate is infinite, however the intensity will continuously decrease as the depth increases. This situation would prompt the question, what level of attenuation is considered to contribute to a reflection peak. Analyzing this one would realize that when the intensity of the X-rays have attenuated to a level at or below the intensity of the noise data, then the diffracted rays would contribute to the same intensity of noise data. In this manner equation 4.1 can be changed to equation 4.2,

$$I_0 / I = S / N = e^{\mu \cdot x} \quad \text{or} \quad I_0 / I = S / N = e^{(\mu/\rho)\cdot\rho\cdot x} \qquad (4.2)$$

where S/N is the signal to noise ratio. Solving equation 4.2 for x, yields equation 4.3.

$$x = \frac{\ln(S/N)}{\mu} \qquad (4.3)$$

The X-rays however need to penetrate the material as incident rays, as well as diffracted rays, therefore the depth that the X-rays will penetrate at this I/I_0 ratio is $x/2$. The previous statement is based on the X-rays being incident perpendicular to the material, since the X-rays are incident at angles other than perpendicular, the depth that the X-rays penetrate is calculated according to equation 4.4

$$d = \frac{x}{2} \cdot \sin(\theta) \qquad (4.4)$$

where d is the penetration depth, x is the total penetration length, and θ is the incident angle. Therefore by substituting equation 4.3, into 4.4 results in equation 4.5.

$$d = \frac{\ln(S/N)}{2\mu} \cdot \sin(\theta) \qquad (4.5)$$

The values for the mass attenuation coefficients have been determined for a number of materials, and records for them are kept by organizations such as the National Institute of Standards and Technology, known simply as NIST. The value of μ for Cu[$k\alpha 1$] is 14.46 ± 0.07 mm^{-1} [43]. Plugging these values into equation 4.5 results in d = 0.147 mm, or 147 μm.

Since this value constitutes the total depth contributing to diffracted rays making up the reflection peak the average depth contributing to the diffraction reflection would only be half of this value, or 0.075 mm, or 75 μm.

4.5 Scanning Procedure

After making all the adjustments for errors several scans were taken. Each scan was allowed to repeat several times, and all the data was accumulated. Many of the scans were observed, in this manner if any gross anomalies were present they would be observed, and corrective action could be taken if necessary. Such corrective action might be to run the scan for a longer time [44-45]. Between each set of scans the adjustment screw was turned one-quarter turn, and the scans repeated. The adjustment screw placed the wafer under a different amount of stress. The first setup put the top portion of the wafer under compressive stress. With each turn of the screw it was expected that the reflection for the sample would shift a little. Since turning the screw in the first setup placed the wafer under compressive stress the lattice parameter in the x-direction would decrease. Because of the Poisson's ratio the lattice parameter in the y-direction would increase. According to Bragg's Law $\lambda/2=d\ \sin\theta$, therefore $d=\lambda/(2\sin\theta)$, and therefore since d is increasing θ should decrease.

4.6 Peak Determination

4.6.1 Peak Height

Peak height can be affected by two main factors, one is shielding, and the other is due to alignment [46]. Shielding is necessary to reduce the intensity of the diffracted X-rays that are incident on the collector. Therefore the height of the reflection is an important factor, as sufficient reflection intensity is an indication of good alignment. In addition a higher reflection will reduce the effect of random errors in the noisy data [47,48]. As this section illustrates, having a sufficient height of the reflection peak is necessary in reducing the uncertainty of the peak location [49]. The amount of

uncertainty of the peak location can be approximately calculated as a function of peak height as in equation 4.6 [50].

$$U_C \approx (2/3)W/\sqrt{C_T} \qquad (4.6)$$

Where U_C is the uncertainty of the peak location, C_T is the total neutron or photon count in the peak and W is known as Full Width at Half Maximum, or FWHM, which is the width of the reflection, measured in radians at half of the reflection height. The uncertainty in the strain as a function of the peak height is illustrated in equation 4.7 [50].

$$U_\varepsilon \approx (1/3)W\cot\theta/\sqrt{C_T} \qquad (4.7)$$

4.6.2 Peak Determination Functions

There are a few common methods for determining the peak of a reflection; these include Pseudo-Voigt method, parabola [51], and COG-center of gravity [52]. The Pseudo-Voigt method fits the diffracted data to a Gaussian function. The parabola method fits the data to a parabola, and the Center of Gravity, or COG, does a weighted average to determine the center of the reflection [52].

An X-ray beam incident on a surface will form a random distribution, which is somewhere between a Lorentzian and a Gaussian distribution, the diffracted X-rays will also form this same distribution. Therefore a reflection from an X-ray diffraction scan will form this same type of distribution. The manner to determine the location of the peak of the reflection would be to fit the data to this same type of distribution. This method of fitting the data is referred to as a Pseudo-Voigt method. It helps to greatly reduce the amount of error in locating the peak of a reflection. There are other methods of locating the peak of a reflection, one other such method is fitting the data to that of a parabola.

Once the data is fitted to the parabola it is a simple matter of algebra to determine the peak. Yet another method of determining the peak of a reflection is called COG, or center of gravity, this is simply dome by finding the weighted average of the data, where the height of each data point is the weight of each data part.

In practice these methods will be done by software, and several methods will be used in order for the user to get a feel of the confidence of the peak locations.

4.6.3 Procedure for Peak Determination

Determining the peak of a reflection is usually done by software, as the process would be very time consuming, and subject to errors, because of the numerous amounts of calculations needed to be done.

With a diffraction scan, the user needs to select the data that will be used in the peak determination. It is important to select enough data so that the entire reflection is included in the data, however selecting too much data will add errors to the result. A good rule to use is to select 3W of data, where W is the width of the reflection at the point that is half of its height, known as full width at half maximum, or FWHM. The first thing that the software does to calculate the location of the peak is to eliminate the noise from the data, which is data from random diffractions; this is seen as the data points that exist between reflections. After the noise data is removed Cu [Kα2] needs to be removed from the data. The X-rays from Cu [Kα] have two wavelengths Cu [Kα1], and Cu [Kα2] that are nearly identical, as a result the two peaks from these wavelengths will occur within the same reflection. In order to correctly locate the peak of the reflection the Cu [Kα2] data needs to be removed from the Cu [Kα1] data. An example of this is shown in Figure 28. Figure 28a is the reflection data before stripping off Cu[kα2], and Figure 28b is after stripping Cu[kα2] off the data. At this point the software will calculate

the peak by using several methods, such as Pseudo-Voigt, parabola, and center of gravity COG.

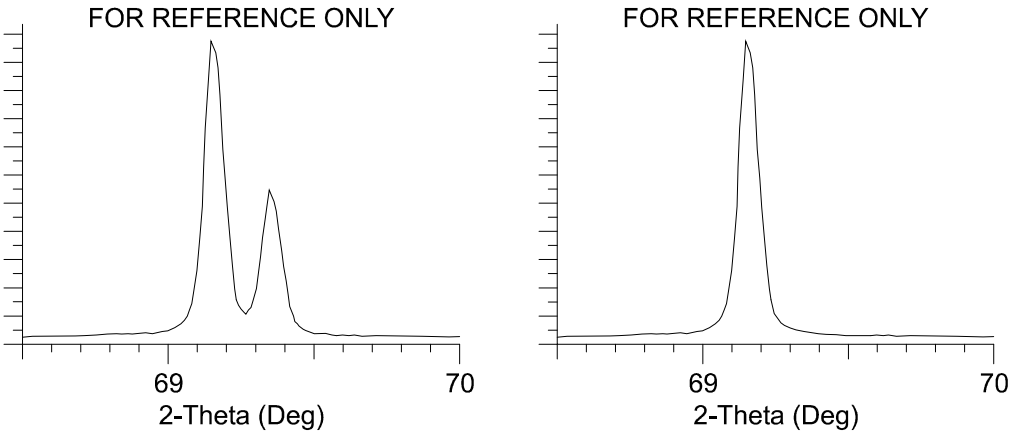

Figure 28. Schematic Representation of a Diffraction Reflection,

(a) Before, and (b) After Stripping Cu[kα2] Off of the Raw Data.

The parabolic fit takes the data and fits it to a parabolic function. Once the data is fit to a parabolic function (i.e. $y = ax^2 + bx + c$) finding the reflection is simply a matter of taking the derivative with respect to x (i.e. $y'=2ax + b$) set $y'=0$, and then simply solve for x, (i.e. $x=-b/2a$).

The center of gravity takes the data, and does a weighted average, as shown in equation 4.8 [53].

$$x=\Sigma f(x_i)\,x_i/\Sigma f(x_i) \qquad (4.8)$$

The Pseudo Voigt method takes the data and fits it to a normal distribution curve. This method assumes scatter of data is due to random errors [54].

4.7 Error Corrections

The vertical alignment done on the setup reduced the amount of error in the vertical direction. However, an additional correction was necessary in order to reduce the errors to a more acceptable degree. Also when the wafer was adjusted in the bending setup, this changed the height of the wafer. As a result it was necessary to make corrections for this adjustment. Copper powder was placed on the wafer. Copper has a known diffraction reflection close to the reflections of the (100) silicon wafer. Because the copper is in the form of a powder its diffraction reflection will not be affected by the bending of the wafer. A picture of the setup with the copper powder placed on the wafer sample is shown in Figure 29; the copper powder is the dark substance in the middle of the sample.

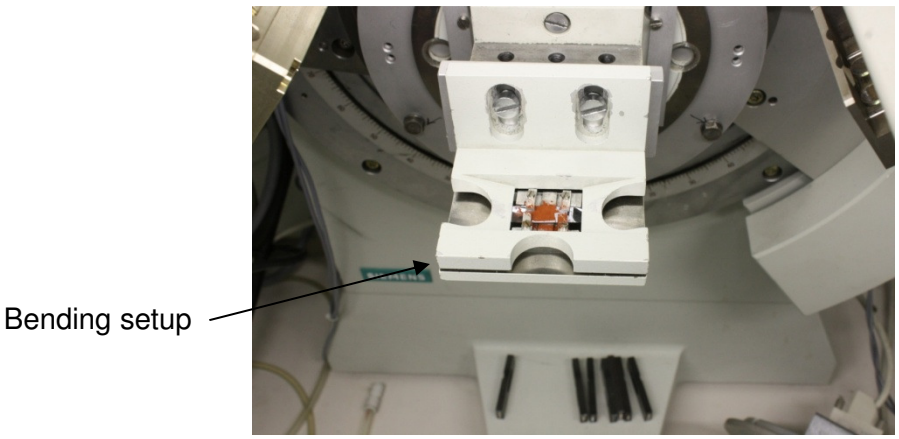

Figure 29. Four-Point Bending Setup for X-Ray Diffraction with Copper Powder Added.

The copper powder may absorb some of the X-rays, but most of the X-rays will pass through the copper powder. Since copper has a known diffraction reflection fairly close to the (100) silicon reflection, the error was corrected by determining the difference between the reflection produced by the copper powder, and where the reflection is

supposed to occur. This difference is then subtracted from the reflection produced by the (100) silicon wafer. Since the reflections occur fairly close to each other this should correct the errors to within an acceptable degree. An illustration of this is shown in figure 32. Note: Figure 30 is not a true scan, the (100) silicon, and (220) copper reflections were scanned separately, as copper needed a higher scan time to get accurate results, the scans were then put together using photo-editing tools, in order to illustrate the method of correcting the reflections using copper powder.

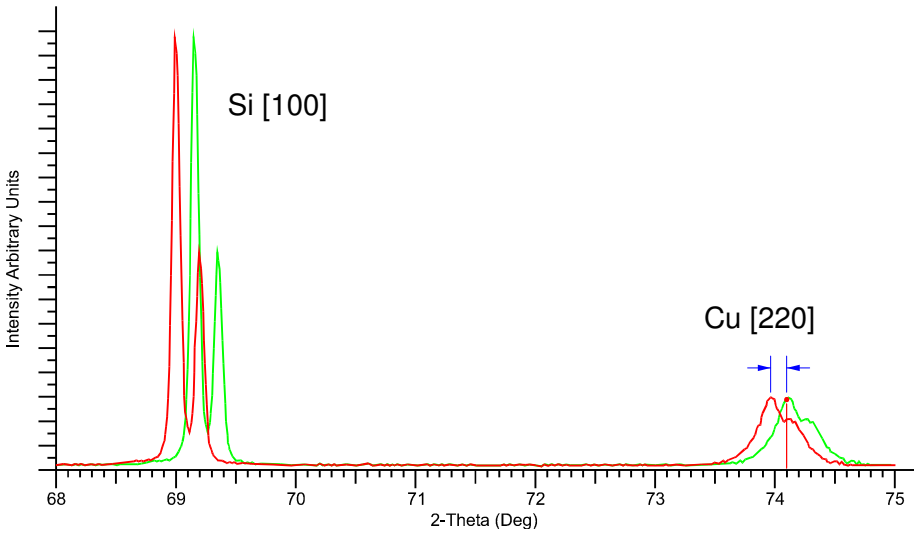

Figure 30. Illustration of Copper Powder Correction.

4.8 In-Situ XRD results

After all the measurements were taken the results were compared to calculations that were made based on the deflections made on the wafer pieces. The strain in the y-direction was calculated from the basic definition of strain, shown in equation 4.9

$$\Delta d/d_0 \qquad (4.9)$$

where d_0 is the unstrained lattice. Equation 4.9 is expanded in order to obtain equation 4.10,

$$\varepsilon_y[\text{XRD}] = (d_{XRD} - d_0)/d_0, \qquad (4.10)$$

where XRD refers to strains determined by X-ray diffraction.

The data that was collected from the X-ray diffraction scans, after correcting for copper powder 220 reflections is shown in Figure 31.

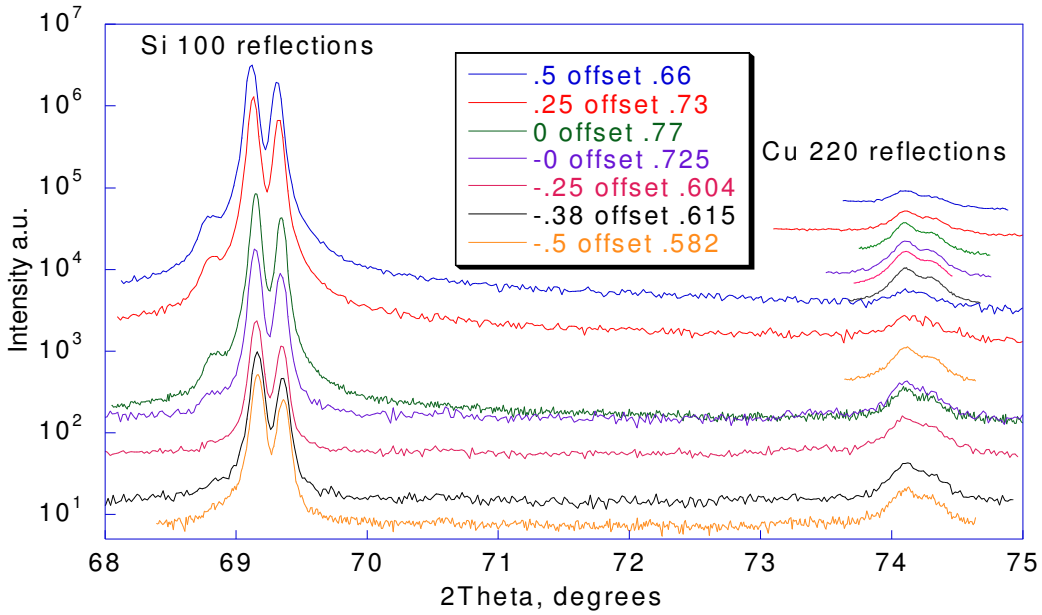

Figure 31. Raw data from the X-ray diffraction scans, after adjusting for copper 220 XRD Reflections, Showing Cu[kα1], and Cu[kα2] Peaks.

After collecting the data the peaks from the reflections were determined using the Pseudo Voigt method, by computer software. Once this was done ε_y[XRD] was determined using equation 4.10.

4.9 Comparison of XRD Results with Calculated Bending Strains

After all the measurements were taken the results were compared with calculations that were made based on the deflections made on the wafer pieces. This data was then compared to the strains that were calculated using the deflections of the wafer piece.

Since the wafer piece is bent using a four-point bending setup, there is a constant radius of curvature between the two inner bending points. The line passing through the center of gravity of the cross-sectional area, perpendicular to the radial line to the center of bending, is the neutral axis. The neutral axis is where there is no longitudinal strain. From here the longitudinal strain (i.e. ε_x) at the surface can be calculated by simple geometry. The longitudinal strain is the ratio of the change in length from the edge of the wafer to the center of the wafer, divided by the length at the center of the wafer. Since both segments create the same angle from the center of bending, the strain is the result of equation 4.11.

$$\varepsilon_x = (S_{edge} - S_{center})/S_{center} = (\pi Redge\,\theta - \pi Rcenter\,\theta)/\pi Rcenter\,\theta \qquad (4.11)$$

In equation 4.11 the common factors π and θ can be factored out resulting in equation 4.12

$$\varepsilon_x = (R_{edge} - R_{center})/R_{center} \qquad (4.12)$$

To determine ε_y one would multiply ε_x by the negative of the Poisson's ratio ($-\nu$.) Since R_{edge} - R_{center} is the thickness (i.e. t), equation 4.13 can be derived from equation 4.12.

$$\varepsilon_y = -\nu t/2r \qquad (4.13)$$

The calculated values of ε_y can be compared to the values of ε_y[XRD] determined by X-ray diffraction. A comparison of the two sets of values are shown in Table 3. From the results shown in Table 3 the calculated values are much closer to the XRD values that were adjusted for copper. The errors for values in compression are much greater than those for tension. One of the possible reasons for this type of error is that the wafer piece may have been under some degree of compression prior to bending. This could have been caused by the lead screw putting pressure on the wafer at this point. This is despite the fact that careful attempts were made, using a piece of paper to move the wafer to ensure that the wafer was not under tension, the lead screw was then tightened in small increments until the wafer could not be moved using a piece of paper.

Table 3. Comparison of Calculated and XRD Strain Results.

Screw turns	2θ deg	d[100Si]	ε_y[XRD]	ε_y[calc]	Variation(%)
0.5 comp	68.993	1.358E-10	4.168E-04	1.390E-03	23.49%
0.25 comp	69.035	1.358E-10	2.406E-04	8.538E-04	30.13%
0	69.103	1.357E-10	0	0	
0	69.149	1.357E-10	4.559E-05	-5.876E-04	
0.25 tension	69.197	1.357E-10	-1.342E-04	-6.086E-04	1.87%
0.38 tension	69.238	1.357E-10	-1.924E-04	-1.132E-03	0.35%
0.5 tension	69.277	1.357E-10	-2.405E-04	-1.613E-03	3.55%

Chapter 5.
System Calibration and Experiment with IONIC-System Stress-Gauge

5.1 IONIC-Systems Profile Calibration

5.1.1 Factory Calibration

It was determined that a calibration for the profile on the stress-gauge should be done. The reason for this is that the stress-gauge and the software were purchased used, and the software may belong to a different stress-gauge.

Each stress-gauge is factory calibrated over its entire measurement range. This calibration is done using a table of 50 data points. These data points are used by the system software in order to convert the reading from the digital readout to distance measurement. Since the stress-gauge unit only needs to measure differences in distance, a digital indicator will be used to make the distance measurements.

5.1.2 Taking Readings

Before doing the calibration of the profile for this stress-gauge, first the stress-gauge needs to have the setup done as described in the section marked IONIC-Systems stress-gauge Setup.

The system measures on both sides of the maximum intensity point, however it does not measure readings at the maximum. The reason for this is that at a relative maximum, the slope is always zero; this means that any change in distance at the maximum will not have any change in the digital reading. At points near the maximum the slope will be very shallow, this means that very small changes in the digital readout

will correspond to large changes in distance. When this happens the uncertainty in the measurements are greatly increased. Therefore in order to reduce the amount of uncertainty in the measurements, data points should be taken far from the maximum intensity point.

The two areas where data points should be taken are referred to by the systems operator manual as the “A”-slope, and the “B”-slope, where the “A”-slope refers to distances less than the distance at the maximum intensity point, and the “B”-slope refers to distances that are greater than the distance at the maximum intensity point.

Readings were taken on the “A” slope. These measurements were taken using a Mitutoyo 543-253 digital indicator. The Mitutoyo digital indicator has a resolution of 0.001 mm (1 μm), and an accuracy of 0.003 mm (3 μm). These instruments work by fixing one end onto a fixed surface, such as the base plate in this instance, the ball end on a movable arm is placed in contact with the surface whose motion is to be measured. The setup for taking these readings was done in a manner to reduce the amount of uncertainty. The digital indicator uses a magnetic base, and a flexible setup in order to hold the digital indicator. The base plate not only serves as a place to attach the magnetic base, but also reduces the motion between the digital indicator, and the fiber-optic bundle. The fiber-optic bundle is mounted to a movable steel spindle. The spindle moves up and down with the probe-gap adjustment, and the fiber-optic bundle moves along with the spindle. This spindle serves a good place to make the measurements with, using the digital indicator. The setup for making these measurements is shown in Figure 32

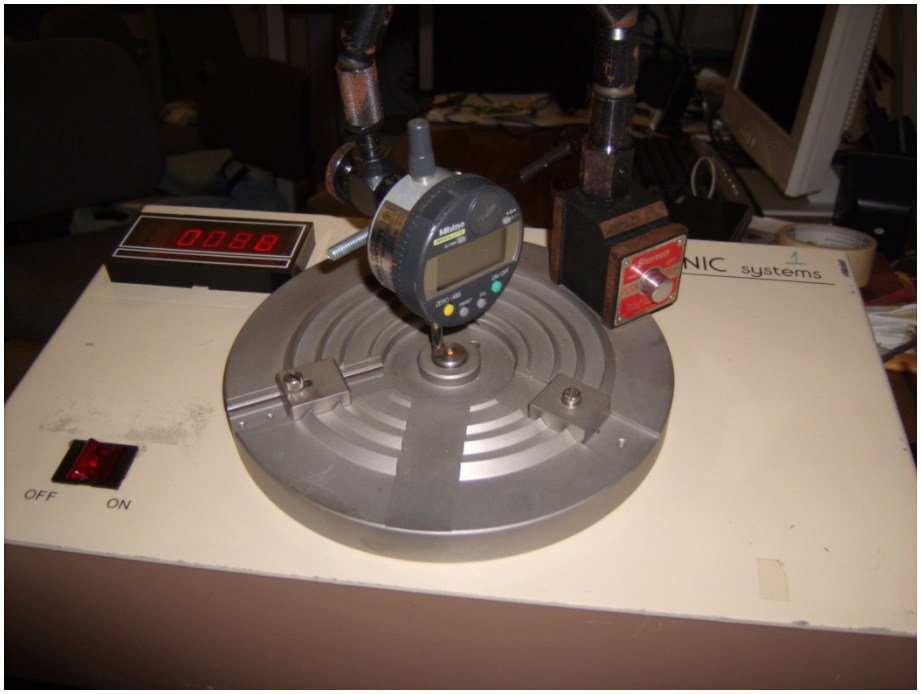

Figure 32. Setup of Digital Indicator on the

IONIC-Systems Stress-Gauge for the Profile Calibration.

Before taking any readings a calibration was done for the digital indicator. This calibration consisted of turning the probe gap adjustment down until the spindle attached to the fiber-optic bundle was about as low as it could go. At this point a marker was placed on the probe-gap adjustment wheel, this would be used to accurately determine whole number of turns of the probe-gap adjustment wheel. The digital indicator was zeroed, and the probe-gap adjustment wheel was turned several turns. At this point a reading on the digital indicator was taken, and the amount of distance that the fiber-optic bundle moved in one revolution of the probe-gap adjustment wheel was determined. Then the setup for the stress-gauge was done as described in the section marked as IONIC-Systems stress-gauge setup, except that after finding the maximum

point the probe gap was not adjusted to a reading of 2500, but left at the reading of 5000, at which point readings were taken on the stress-gauge.

When the setup was done before doing this profile calibration, the probe-gap was not adjusted to obtain an output reading of 2500 as described in the operator's manual, but instead the probe-gap adjustment was left at the maximum intensity point where it had a value of 5000 on the digital readout. This was because the readings were taken over the entire range. This profile calibration measures changes in distance so the initial distance measurement was given a value of zero. Each measurement taken was compared to the values obtained from the software, in order to give a feel for the level of confidence in the readings. The initial reading from the digital output on the stress-gauge was entered into the software as a "Before"-reading, this "Before"-reading would remain for the entire profile calibration. Each successive reading would be entered into the software as an "After"-reading, this would give distance values output from the software that would correspond to distance values that were taken manually. The values from the software should be within an acceptable amount of tolerance from the values that were taken manually. At each measurement the probe-gap adjustment wheel was turned one-eighth of a turn, the output from the stress-gauge digital readout was entered into the software as an "After"-reading, the distance value was calculated by the software, and all the values, including the digital output from the stress-gauge, the number of turns of the probe-gap adjustment wheel, and the result from the software were entered into a spreadsheet file. A total number of 25 data points were taken for each profile calibration. The profile calibration was repeated twice on the same wafer, and another two profile calibrations were done on another wafer, and the results were compared.

5.1.3 Profile Calculation

The data used in the profile calibration are shown in Figure 33. As can be seen in Table 4 the software has virtually no variance in the data, as is expected, however there is some amount of variance from one profile to another, as well as the average profile deviating from the software profile.

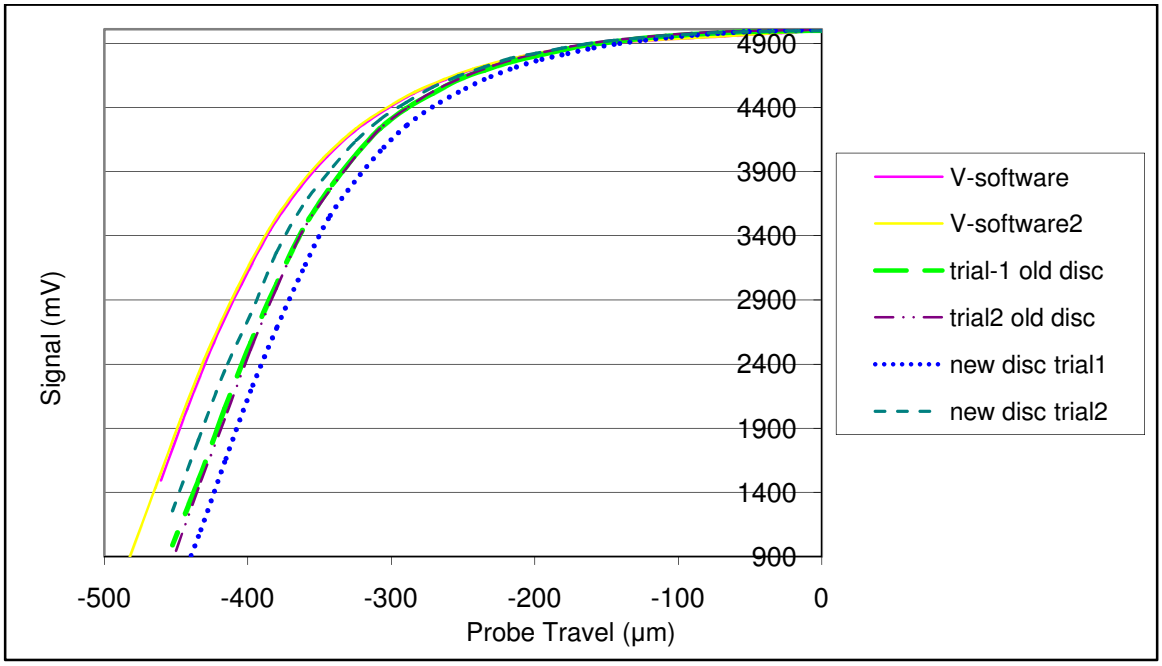

Figure 33. Data Used in Stress-Gauge Profile Calibration.

For each profile that was taken a linear regression was done, using data points that appeared to be within the linear region. The selection of data points was simply done visually, taking notice of where the data appeared to deviate from a linear function. The linear regression was done using the built-in functions of the spreadsheet software. The linear regression resulted in a total of five slopes, including the slope for the software. The other four slopes were for each of the profile calibrations. Since the software calculates the outputs based on internal formulas, no variation is expected with

the software, however the profiles for the samples that were taken manually a variance was expected, and an analysis of this variance was done.

An average was taken for all the slopes, and a standard deviation was calculated. Also the difference between the average slope, and the slope obtained from the software was calculated. This is shown in Table 4.

Table 4. Results From Stress-Gauge Profile Calibration.

Slope	Source
25.49897	Software
26.92747	Disc1 Trial1
27.73408	Disc1 Trial2
28.62908	Disc2Trial1
25.20376	Disc2Trial2

Results	
27.12359	Slope Average
1.456413	Standard-Deviation
1.624625	Slope Difference from Software

5.2 IONIC-System Experiment

5.2.1 IONIC-Systems Stress-Gauge Readings

After doing the profile calibration measurements were taken on a wafer that was placed under a load. First a setup was done for the wafer that was being used, as described in the section marked IONIC-Systems stress-gauge Setup. The load that was placed on the wafer was from common metal weights that were placed on the center of the wafer. The weights used were 1g, 25g, 100g, and both the 1g and 25g weight. The deflection was then determined using the IONIC-Systems stress-gauge, and the

deflection of the wafer was determined. The readings obtained from the IONIC-Systems stress-gauge are listed in Table 5.

Table 5. Readings From IONIC-Systems Stress-Gauge for Various Weights Added, and the Corresponding Displacements.

Weight	Digital output	Displacement
Before (no weight)	2543	0 µm
1g	2523	0.7373654 µm
25g	2026	19.060896 µm
26g	2006	19.798261 µm
100g	307	82.437452 µm

5.2.2 Wafer Deflection Equation

The displacements for the various weights were also calculated for small deflections of a flat circular plate. In order to calculate the deflection of the wafer under the load, the type of loading needs to be determined. The knife edge on the IONIC-Systems stress-gauge causes the wafer to be simply supported at the outer edge. The type of loading caused by the weights needs to be determined.

The weights are made from machined aluminum, and each weight has a flat area on the bottom with a diameter ofabout 0.625 in. Since the weights have a flat area on the bottom it seems that the loading should be that of a circular area in the center of the wafer, as shown in Figure 34a. In this case the deflection from the weight would be according to equation 5.1 [55], where the deflection is based on a uniform load over a very small central circular area, and edge simply supported. However the machining process may have produced a lip as shown in Figure 34b. In this case the deflection would be according to equation 5.2 [55], where the deflection is from a uniform annular

line load, as shown in Figure 34c. One test to see if a lip is present would be to feel the bottom area of the weight with the fingernail, however a person is only able to sense approximately one-half of one thousandth of an inch, or 0.0005-in [12.7μm], this would mean that it is possible that a small amount of lip could be present without being able to be detected by simple means. As a result the type of loading will be considered to be somewhere between the two types of loading. Both types of loading will be calculated, which will result in an upper, and lower bounds for the calculations.

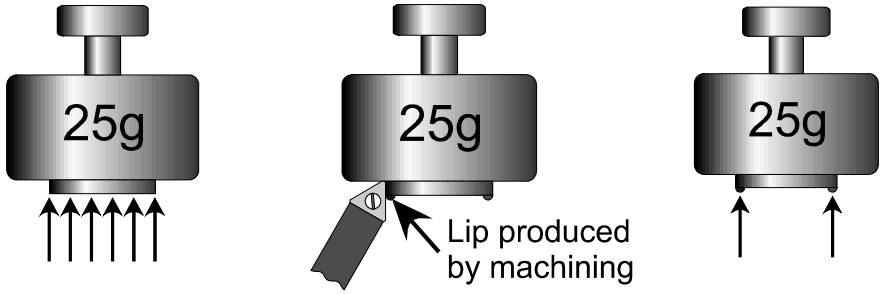

Figure 34. (a) Weight Producing a Small Circular Area Load on the Wafer.

(b) Lip Produced by Machining Process.

(c) Load from Weight Concentrated Along Outer Edge of Weight-Flat.

The equation for small circular area loading is equation 5.1, and the equation for a load concentrated along the weight-flat circumference is equation 5.2, equations 5.3-5.5 are necessary in order to use equations 5.1, and 5.2 [55, 56,].

$$y_{Max} = \frac{-Wa^2}{16\pi D}\left(\frac{3+\nu}{1+\nu}\right) \quad \text{(5.1) case-16a, small circular area load}$$

$$y_{Max} = \frac{-Wa^2}{2D}\left(\frac{L_9}{1+\nu} - 2L_3\right) \quad \text{(5.2) case-9a, annular line load}$$

$$L_9 = \frac{r_0}{a}\left\{\frac{1+\nu}{2}\ln\left(\frac{a}{r_0}\right)+\frac{1-\nu}{4}\left[1-\left(\frac{r_0}{a}\right)^2\right]\right\} \quad (5.3)$$

$$L_3 = \frac{r_0}{4a}\left\{\left[\left(\frac{r_0}{a}\right)^2+1\right]\ln\left(\frac{a}{r_0}\right)+\left(\frac{a}{r_0}\right)^2-1\right\} \quad (5.4)$$

$$D = \frac{Et^3}{12\left(1-\nu^2\right)} \quad (5.5)$$

where W = weight of load, a = radius of support, E = modulus of elasticity, ν = Poisson's ratio, and r_0 = radius at outer edge of load.

5.2.3 Variation Caused by Anisotropic Properties

As mentioned earlier, single crystal silicon is not an isotropic material, however the biaxial modulus in the {100} plane is a constant. The value of the biaxial modulus for (100) silicon plane is B_{100} = 179.4 GPa [19], where the biaxial modulus in equation 2.3 is repeated here.

$$B = \frac{E}{(1-\nu)} \quad (2.3) \text{ repeated}$$

Since the biaxial modulus is a constant it is possible to have an equation for the deflection as a function of the elastic properties as $y_c = f(B,\nu)$, as opposed to $y_c = f(E,\nu)$. Note that since $1-\nu^2 = (1+\nu)(1-\nu)$, the value for D, when B is substituted for $E/(1-\nu)$ is given in equation 5.5.

$$D = \frac{Et^3}{12\left(1-\nu^2\right)} \quad (5.5)$$

As stated in the previous section the biaxial modulus is a constant in the {100} plane, but the modulus of elasticity, and the Poisson's ratio are not. The modulus of

elasticity ranges from 130 GPa, to 169 GPa, in the {100} plane, this is a ratio of 1.3 or a variation of 30%. The Poisson's ratio on the other hand ranges from 0.064, to 0.28, in the {100} plane, this is a ratio of 4.375, which is a ratio greater than four to one. This range of an elastic constant for the Poisson's ratio in the {100} plane would cause a significant amount of error in the calculations. The biaxial modulus takes both of these elastic properties into account, and is constant throughout the {100} plane, however the Poisson's ratio is still part of the equation for displacement of the wafer. For the value of D, which is used in the calculation of the displacement, this range would be $(1+\nu_{MAX})/(1+\nu_{MIN})$, this is a ratio of 1.28/1.064, or 20% variation. This still leaves Poisson's ratio terms in the deflection calculations. When calculating the deflection using the maximum, and the minimum Poisson's ratio the result varies by 6.5%, and 7%, for case-9a, and case-16a respectively. This result can change by as much as 7% due to the difference in Poisson's ratio.

5.2.4 IONIC Stress-Gauge Error Analysis

The output for the IONIC stress-gauge is in mV, therefore the deflection caused by a 1 mV change in output is approximately 0.037 μm, therefore the displacement resolution of the stress-gauge is approximately 0.04 μm. The IONIC stress-gauge has a precision to tolerance ratio of 0.28 [57], and from the profile calibration the standard deviation is 1.456413 mV/μm, multiplying this by the slope of the IONIC stress-gauge gives a tolerance of 0.687 μm.

5.2.5 Wafer Deflection Results

A (100) silicon wafer was placed in the IONIC stress-gauge, and measurements were taken. These measurements that were taken were compared to the calculations mentioned previously, as shown in table 6.

Table 6. Wafer Deflection Measurements and Calculations.

Weight	Digital output	Displacement	Case-9a	Case-16a
none	2543	0 µm	0 µm	0 µm
1g	2523	0.7373654 µm	0.7249038 µm	0.77665 µm
25g	2026	19.060896 µm	18.122594 µm	19.4162 µm
26g	2006	19.798261 µm	18.847498 µm	20.1928 µm
100g	307	82.437452 µm	72.490378 µm	77.6647 µm

The percent errors from the measured values were also calculated as shown in table 7.

Table 7. Errors From Deflection Calculations.

Weight	%error-9a	%error-16a
none	NA	NA
1g	1.69%	7.14%
25g	4.92%	7.14%
26g	4.80%	7.14%
100g	12.07%	7.14%

Chapter 6.
Conclusions and Future Work

The methods of XRD to determine the strain in the material show a potential in being able to determine distortions in X-ray mirrors. X-ray diffraction has been used successfully to determine the stress by measuring the lattice spacing between crystallographic planes. These tests however were inconclusive because of the errors induced from the play in the bending mechanism. By using a more careful means of determining the curvature in the wafer sample it may be possible to more precisely define the results. The IONIC stress-gauge mentioned in this paper is one means to be able to determine the curvature in order to better compare the XRD results with other curvature methods. However there needs to be a means to measure the deflection of the sample that causes a change in curvature of the sample in the bending fixture by either the IONIC stress-gauge, or some other mechanism.

Another reason for the cause of variation between the calculated strain, and the XRD strain is in zeroing the sample. The variation in one direction has a very low variation, but there is significant variation in the other direction, which seems to suggest that there was either play in the setup, or some initial stress in the direction with greater variation.

Another method that was mentioned in this paper was using the $\sin^2\psi$ method. The $\sin^2\psi$ method is used to determine the stress in the layers deposited on the mirror substrate, then by using the Stoney's equation to determine the change in curvature after the stress was determined using the $\sin^2\psi$ method. The $\sin^2\psi$ method was used in

this paper to determine the stress in a tungsten film, not on X-ray mirrors, however the stress in the layers could be able to be measured using the same methods. These methods were not pursued during this research due to lack of time, and other constraints. However, these methods show promise in being able to determine changes in curvature of X-ray mirrors.

References

1. C. Tang, M. Miller, & D. Laundy, CLRC *Technical Report DL-TR-96-003. Daresbury Laboratory*, Warrington, England. (1996).

2. C. Michaelsen, P. Ricardo and D. Anders, *Improved graded multilayer mirrors for xrd applications*, Institute of Materials Research, GKSS Research Center, vol 42, 2000, pp 308-320

3. N. Gurker, R. Nell, G. Seiler, and J. Wallner, *A tunable focusing beamline for desktop X-ray microtomography*, Institut fu¨r Angewandte und Technische Physik, Technische Universita¨t Wien, vol 70, 1999.

4. C. Rogers, D. Mills, and W. Lee, *Performance of a liquid-nitrogen-&oled, thin silicon crystal monochromator on a high-power, focused wiggler synchrotron beam*, Scientific Instruments, v 66, pp 3494-9, 1995.

5. M. Rubel, P. Brunsell; R. Duwe, J. Linke, *Molybdenum limiters for Extrap-T2 upgrade: Surface properties and high heat flux testing, Fusion Engineering and Design*, v 49-50, p 323-329, 2000

6. D. Meyer,T. Leisegang, A.A. Levin, P. Paufler, A.A. Volinsky, *Tensile crack patterns inMo/Si multilayers on Si substrates under high-temperature bending*, Institut für Strukturphysik, Fachrichtung Physik der Technischen Universität, Materials Science & Processing, pp 303-305, 2003.

7. T. Burke, D. Huxley, R. Newport, R Cernik, An *in situ X-ray diffraction method for the structure of amorphous thin films using shallow angles of incidence*, Review of Scientific Instruments, v 63, pp 1150-2, 1992.

8. J. Harvey, P. Thompson, C. Vernold, *Understanding surface scatter effects in grazing incidence X-ray synchrotron applications*, Proceedings of the SPIE - The International Society for Optical Engineering, v 3447, pp 94-100, 1998

9. M. Rowen, J. Peck, T Rabedeau, *Liquid nitrogen cooled X-ray monochromator for high total power loads*, Nuclear Instruments and Methods in Physics Research, Section A: Accelerators, Spectrometers, Detectors and Associated Equipment, v 467-468, p 400-403, July 21, 2001

10. C. Rogers, *High heat flux X-ray monochromators: What are the limits?, Proceedings of SPIE - The International Society for Optical Engineering*, v 3151, pp 201-207, 1997, High Heat Flux and Synchrotron Radiation Beamlines

11. H. Goebel, inventor; 1994 Dec 13. *X-ray diffractometer*. United States patent 5,373,544,

12. Y.C. Lin, J.Y. Li, W.T. Yen, *Low temperature ITO thin film deposition on PES substrate using pulse magnetron sputtering*, Applied Surface Science, v 254, pp 3262-8, 2008

13. A A. Volinsky, *The Role of Geometry and Plasticity in Thin, Ductile Film Adhesion*, University of Minnesota, 2000

14. A. Zanattaa,F. Ferri, *Crystallization, stress, and stress-relieve due to nickel in amorphous silicon thin films*, 2007, pp

15. H. Yu, J. Hutchinson, *Delamination of thin film strips*, Thin Solid Films, 2003, pp 54-63

16. J. Lu, *Handbook of Measurement of Residual Stresses. Lilburn*, GA: Fairmont Press, 1996.

17. P. Waters & A.A. Volinsky, *Stress and Moisture Effects on Thin Film Buckling Delamination*, Experimental Mechanics, vol. 47, 2007, pp 163-170

18. W. O'Mara, R. Herring, L. Hunt, *Handbook of semiconductor manufacturing technology*, William Andrew Inc., 1990

19. M. A. Hopcroft, *Silicon Micromechanical Resonators for Frequency References*, Ph.D. dissertation, Stanford University, Stanford, CA USA, 2007.

20. M. A. Hopcroft, *What is the Young's Modulus of Silicon*, 2006

21. A. Jachim, *Orthotropic Material Properties of Single Crystal Silicon*, 1999

22. R.P. Vinci, E.M. Zielinski, J.C. Bravman, *Thermal strain and stress in copper thin films*, Thin Solid Films, vol. 262, 1995, pp 142-153

23. W. Callister Jr., *Materials Science and Engineering-7th Ed.*, John Wiley & Sons, Inc, 2007

24. O. Anderoglu, *Residual Stress Measurement Using X-ray Diffraction*, Mechanical Engineering, Texas A&M University, 2004

25. Noyan I. C. and Cohen J. B., *Residual Stress: Measurements by Diffraction and Interpretation*, 1987, Springer-Verlag, New York.

26. Hauk V., *Structural and Residual Stress Analysis by Nondestructive Methods*, 1997, Elsevier, Amsterdam.

27. Winholtz R. A. and Cohen J. B., *Aust. J. Phys.*, 41, 189-199 (1988).

28. G. Beck, S. Denise, A. Simons, *International Conference on Residual Stresses*, Elsevier Applied Science, 1989

29. Slaughter W, *The Linearized Theory of Elasticity*, Boston: Birkhauser; 2002.

30. Nye J. F., *Physical Properties of Crystals: Their Representation by Tensors and Matrices*, 1985, Clarendon Press, Oxford.

31. Reddy JN, *Mechanics of Laminated Composite Plates*, Boca Raton, FL: CRC Press; 1997.

32. G.G. Stoney, *The Tension of Metallic Films Deposited by Electrolysis*, Proc. Roy. Soc. London A 82, pp. 172-175 (1909)

33. M. A. Moram, M. E. Vickers, M. J. Kappers, and C. J. Humphreys, *The effect of wafer curvature on X-ray rocking curves from gallium nitride films*, 2008.

34. Barber, K. Samuel; Soldate, Paul; Anderson, H. Erik; Cambie, Rossana; McKinney, R. Wayne; Takacs, Z. Peter; Voronov, L. Dmytro; Yashchuk, V. Valeriy, *Development of pseudorandom binary arrays for calibration of surface profile metrology tools, Journal of Vacuum Science and Technology B: Microelectronics and Nanometer Structures*, v 27, pp 3213-3219, 2009.

35. J.H. Selverian, *Errors in curve fitting of profilometer data, Journal of Vacuum Science & Technology A (Vacuum, Surfaces, and Films)*, v 10, pp 3378-82, 1992

36. G. Chong, *Smoothing noisy data via regularization: statistical perspectives*, Inverse Problems, v 24, pp 034002 (20 pp.), June 2008.

37. D. Koutsoyiannis, *Broken line smoothing: a simple method for interpolating and smoothing data series*, Environmental Modelling & Software, v 15, pp 139-49, 2000.

38. A.J. Rosakisa, R.P. Singh, Y. Tsuji, E. Kolawa, N.R. Moore Jr., *Full field measurements of curvature using coherent gradient sensing: application to thin film characterization*, Thin Solid Films, vol. 325, 1998, pp 42–54

39. J Rachwal, A A. Volinsky, H Stöcker, D. Meyer, *X-ray Stress Analysis of Silicon Wafers Under Four-point Bending*, Technischen Universität, Dresden, Germany, , University of South Florida,2007

40. A.A. Benzerga, N.F. Shaver, Scale *dependence of mechanical properties of single crystals under uniform deformation*, Scripta Materialia, vol. 54, 2006, pp 1937-1941

41. K. Bretzfield, F. Woeste, *Joist Curvature versus Sheathing Curvature and the Probable Role of each on Ceramic Tile Performance*, 2008, TTMAC HARDSURFACE Magazine.

42. V. Thomsen, D. Schatzlein, D. Mercuro, Tutorial: *Attenuation of X-rays by matter, Spectroscopy*, v 20, pp 22-25, 2005.

43. L. Gerward, *X-ray attenuation coefficients and atomic photoelectric absorption cross sections of silicon*, Journal of Physics B (Atomic and Molecular Physics), v 14, pp 3389-95, 1981.

44. J Taylor, *Error Analysis The Study of Uncertanties*, University Science Books, 1982

45. R Figiola, D Beasley, *Theory and Design for Mechanical Measurements 4th-Ed.*, John Wiley & Sons, Inc., 2006

46. Philip J. Withers, Mark R. Daymond and Michael W. Johnson, *The precision of diffraction peak location*, 2001

47. Webster P. J. and King W. P., *Optimization of neutron and synchrotron data collection and processing for efficient Gaussian peak fitting. Engineering Science group Technical Report ESG01/98*, The Telford Institute of Structures and materials Engineering, University of Salford, March 1998.

48. H. Toraya, *Estimation of errors in the measurement of unit-cell parameters*, 2001

49. E.N. Dulov, D.M. Khripunov, *Voigt lineshape function as a solution of the parabolic partial differential equation*, Radiative Transfer, vol. 107, 2007, pp 421-428

50. M. E. Fitzpatric, A. Lodini, *Analysis of Residual Stress by Diffraction using Neutron and Synchrotron Radiation*, Boca Raton, FL: Taylor & Francis, 2003

51. P.. Prevéy, *The Use of Pearson VII Distribution Functions in X-ray Diffraction Residual Stress Measurement*, vol. 29. 1986, pp 103-111

52. E.N. Dulov, D.M. Khripunov, *Voigt lineshape function as a solution of the parabolic partial differential equation, Radiative Transfer*, vol. 107, 2007, pp 421-428

53. W. Parrish and J. I. Langford, *International Tables for Crystallography*, Volume C: Mathematical, Physical and Chemical Tables, 2004

54. D Balzar, *Voigt-function model in diffraction line-broadening analysis*, University of Colorado, 1999

55. Y. Warren, *Roark's Formulas for Stress and Strain. 6th ed.,* New York: Mcgraw-Hill, 1989

56. P. Walter, *Formulas for Stress, Strain, and Structural Matrices*, Charlottesville, Virginia: John Wiley & Sons, Inc., 1994

57. V.S. Dharmadhikari, *Statistical approach to parameter study of stress in multilayer films of phosphosilicate glass and silicon nitride*, Journal of Vacuum Science & Technology A (Vacuum, Surfaces, and Films), v 9, pp 2497-502, 1991.

Appendices

Apendix A

A-1 IONIC-Systems Stress-Gauge

The IONIC-Systems stress-gauge determines the residual stress in the thin film on a wafer based on the change in curvature of the wafer; it does this by taking two measurements, before, and after processing in order to determine the deflection caused by processing the wafer. This system operates by measuring the light intensity reflected off the back side of the wafer. The IONIC-System can make very precise measurements using this method. This system determines the deflection at the center of the wafer; as a result changes in curvature over the wafer diameter cannot be determined. The use of a light beam for measurement means that the measurements are nondestructive. Readings are taken before and after the wafer is processed, thus a change in curvature is determined. After the deflection is determined, the stress can be calculated using the deflection, and the properties of the wafer.

The back panel of the IONIC-Systems stress-gauge contains the probe-gap adjustment, and lockdown, the lamp intensity adjustment, and lockdown, and the computer interface shown in Figure 35. The probe-gap adjustment consists of a large thumbwheel mounted on a threaded shaft that provides the adjustment; the lockdown for the probe-gap consists of a threaded wheel that tightens against the adjustment wheel. Next to the wheel are markings to indicate the direction for increasing, and decreasing the probe-gap, these markings are labeled as “INCR,” and “DECR”, respectively. The back panel also contains a RS-232 computer interface, which allows the user to link the output reading to a computer.

Figure 35. Back panel of IONIC-systems stress-gauge.

The top face of the IONIC-System contains the power switch, digital readout, and a base-plate. The power switch controls the power to the stress-gauge. The digital readout is a four digit readout related to the reflected light intensity. This readout is a measure of the voltage reading of the internal sensor, where a reading of 5000 corresponds to 5 Volts. The user does not need to relate this voltage to a light intensity, there is software for the user to input the readout on the system to determine the distance of the fiber-bundle to the back of the wafer.

The top of the IONIC-Systems stress-gauge has a base-plate, with a fiber optic bundle, a series of knife edges, and positioning blocks as shown in Figure 36. The fiber optic bundle is at the center of the base plate; it can be adjusted up or down, and is used to make the measurements to determine the deflection of the wafer center. The knife edges are the series of concentric circles surrounding the fiber-optic bundle. These knife edges hold the wafer near the outer edge of the wafer, so that the measurement is

over most of the wafer's diameter. The knife edges allow for different size wafers, and each series of knife edges is at a different height to allow clearance for larger wafers. The base plate also contains three different positioning blocks. These positioning blocks can be placed accordingly to allow for different size wafers. These positioning blocks along with the knife edge constrain the wafer for accurate location. These positioning blocks are located at the 12-o'clock, 4-o'clock, and 8-o'clock position. The positioning block at the 4-o'clock position is fixed, while the other two are spring loaded. The two spring-loaded blocks have different spring constants, so that one will be seated, while the other is under compression.

Figure 36. Top of IONIC-Systems stress-gauge.

The wafer needs to be fixed in all degrees of freedom to help ensure accuracy in measurements.

The knife edges constrain the wafer to a plane allowing only three degrees of freedom, such as the x-direction, y-direction, and rotation. The positioning block at the four-o'clock position is fixed in place and constrains the wafer in the y-direction. The other two positioning blocks are spring mounted, the positioning block at the 8-o'clock position has a spring with a much stiffer spring constant than the one at the 12-o'clock position, and therefore the positioning block at the 8-o'clock position will determine the position in the x-direction. This leaves only one degree of freedom remaining, the angular position. The major flat on the wafer is positioned against the block at the 8-o'clock position, and the user needs to press the positioning block at the 12-o'clock position several times in order to properly seat the flat of the wafer against the positioning block at the 8-o'clock position. After this is done the wafer is properly positioned. In this manner two of the positioning blocks are placing spring load on the wafer, in order to help ensure that the wafer will not drift out of position.

The IONIC-System uses fiber-optic bundle to make measurements. The fiber optic bundle is very sensitive, and any contact can cause damage, care to avoid contact with the fiber optic bundle is necessary. The fiber optic bundle contains optical fibers half of these optical fibers transmit light, and half of the optical fibers receive light. The measurement is taken by transmitting light from some of the optical fibers onto the back of the wafer, the light is then reflected back to the optical fiber bundle, and the receiving fibers transmit the light reflected back to a light sensor that reads the intensity. The light that is reflected back is compared to an intensity reading directly from the light source, in order to reduce certain types of errors. The light being reflected has a focal point within the range of measurement, the light intensity will maximize at this focal point, and therefore there is a relative maximum within the range of measurement. Reading cannot

be taken at this maximum point, because the derivative of this measurement with respect to light intensity will be zero. Readings may be taken on either side of the maximum reading, the manual refers to these two sides of the maximum as slopes A, and B.

In order to calculate the stress on the wafer the IONIC-Systems stress-gauge comes with software in order to do the calculation using the digital readout. The software is a DOS based program that is included with the IONIC-Systems stress-gauge. The software is on a 3.5-inch floppy disk, and contains all the system files necessary to run the software. The program file for the software is STRESS.EXE. Launching STRESS.EXE brings the user to the main menu, where there are four options available, 1-Stress measurement, 2-Stress calculation, 3-Others, and End. End simply exits the program as suggested. Stress measurement labeled as option-1 has five main options, Before, After, Wafer, View, and Esc, where Esc returns to the previous menu. Before any measurements are taken, the user needs to enter a name for the wafer; this way information for several wafers may be stored at one time.

Choosing the option marked “Wafer” allows the user to enter a name for the wafer. Each wafer must have some name to it before entering values for stress measurement into the software. Pressing “W”, while at the Stress-Measurement screen selects this option, and brings up a dialog box, which prompts the user to enter a name for the wafer. The user can enter any name that the user deems appropriate to identify the wafer, into the dialog box, and then press the enter key. The name that the user selects is limited to a certain number of characters.

The user should choose option marked “Before”, provided that the wafer has been given a name to identify it. The method to enter a name for a wafer is given in the

previous paragraph. Pressing “B”, while at the Stress-Measurement screen selects this option, and brings up a dialog box, which prompts the user to enter a value taken from the digital readout on the IONIC-System stress-gauge. After the value is entered the user should press the return key, to return to the previous menu. It is important that the user take a measurement, and enter this value into the software before any processing is done on the wafer. If no measurement is taken before any processing is done on the wafer, the software will not be able to properly determine the stress in the wafer.

The user should choose option marked “After”, when the wafer has been processed, and a measurement has been taken from digital readout of the IONIC-System stress-gauge. Pressing “A”, while at the Stress-Measurement screen selects this option, and brings up a dialog box, which prompts the user to enter a value taken from the digital readout on the IONIC-Systems stress-gauge. After the value is entered the user should press the return key, to return to the previous menu. If the user has entered before, and after measurements into the software at this point, the software will be ready to calculate a value for the stress on the wafer. By determining the difference between the two readings, a change in the wafer curvature can be determined.

The light intensity that is being measured may change in two ways, one is due to a change in distance of the fiber bundle from the wafer, and the other is due to changes of the reflectivity in the back of the wafer. For this reason the back side of the wafer is used for measurements, and it is necessary to mask of the area on the back of the wafer that will reflect the light to make measurements.

The stress-gauge constantly measures the light source directly, and compares this reading to the light intensity that is being reflected off the back side of the wafer. By

making the measurements in this manner, errors due to fluctuations in the lamp intensity either because of age, or line voltage fluctuations are greatly reduced.

A-1.1 IONIC-Systems Stress-Gauge Calibration Setup

In order to setup the IONIC-Systems stress-gauge the unit needs to warm up for a period of 72-hours before measurements. There are different sets of threaded holes to which the positioning blocks can be installed depending on the size of the wafer being used. The wafer should be placed so that the back side of the wafer, that is the side that will not be processed is down, that is in contact with the appropriate set of knife edges, and facing the optical-bundle. The major flat on the wafer should be flush with the 8-o'clock positioning block, and the user should use the procedure described in the previous section to ensure that this is properly done. Care needs to be used to avoid touching the optical-bundle, to avoid damage that may yield inaccurate results. After the wafer is positioned, a reading should be taken, and the wafer removed, then reinserted several times using the correct seating procedure. The user needs to check the reading each time the wafer is seated, and ensure that a repeatability of ±10 counts on the digital readout is reached.

With the wafer properly seated, the probe-gap adjustment needs to be unlocked, and the user should adjust the probe gap so that the reading on the indicator is increasing. If when adjusting the probe-gap the readout decreases the user should make the adjustment in the other direction, also if the digital readout starts to approach the maximum reading, the user should unlock the lamp intensity adjustment, and adjust the lamp intensity to a value that is well within the range of the digital reading, a value of 5000 is a good suggested value. The user should continue the adjustment until the

readout reaches a maximum. The user should obtain the maximum by continuing the adjustment past the maximum point until the readout starts to decrease, then reverse the adjustment until the returning to the previous maximum value. At this point the user should unlock the lamp intensity adjustment, and adjust the lamp intensity so that the digital readout is within ±10 counts of 5000, and then lock the lamp intensity adjustment, ensuring that the readout does not drift out of specs in doing so. This is best done by first setting the value to 5000, and locking down the adjustment first, and noting the amount of drift that occurs from doing so. Then the user should unlock the lamp intensity again, and adjust the lamp intensity so as to account for the amount of drift that occurs while locking the adjustment down. At this point the user should adjust the probe-gap in the decreasing direction, that is so that the gap between the fiber optic bundle, and the back side of the wafer will be decreasing. Note that turning the gap adjustment in either direction will cause a decreasing value in the digital readout, so the user should refer to the back of the machine to ensure they are moving the fiber-optic bundle in the “DECR”-direction, indicating a decreasing gap between fiber-optical bundle, and wafer. The adjustment should be made to obtain a digital readout within ±100 counts of 2500 on the digital readout. The probe-gap adjustment needs to be locked down at this point. The wafer is ready to make a reading. The user should record this reading on the digital readout, and enter this value into the software for the IONIC-Systems stress-gauge, this should be entered as the before reading in the software. The previous section labeled IONIC-Systems software describes the manner of entering before, and after values.

A-1.2 Taking a Measurement on the IONIC-Systems Stress-Gauge

In order to take a measurement on the IONIC-Systems stress-gauge the setup needs to be done for the system, as described in the previous section. Once the setup is done a before-reading should have been taken, before the wafer is processed. The back of the wafer should be masked in order to avoid changing the reflectivity of the back of the wafer, where the IONIC-Systems stress-gauge will take a measurement. Once the wafer is processed the wafer should be placed on the stress-gauge knife edge, and the wafer needs to be seated by repeatedly pushing, and releasing the block at the 12-o'clock position, as described in the previous section. The user should take the reading from the digital readout, and enter it into the software as an after reading.